INSTITUTE OF PHYSICS PUBLISHING and INTERNATIONAL ATOMIC ENERGY AGENCY NUCLEAR FUSION

Nucl. Fusion **44** (2004) 134–153 PII: S0029-5515(04)71999-7

High-speed imaging of edge turbulence in NSTX

S.J. Zweben, R.J. Maqueda[1], D.P. Stotler, A. Keesee[2], J. Boedo[3], C.E. Bush[4], S.M. Kaye, B. LeBlanc, J.L. Lowrance[5], V.J. Mastrocola[5], R. Maingi[4], N. Nishino[6], G. Renda[5], D.W. Swain[4], J.B. Wilgen[4] and the NSTX Team

Princeton Plasma Physics Laboratory, Princeton, NJ, USA
[1] Los Alamos National Laboratory, Los Alamos, NM, USA
[2] West Virginia University, Morgantown, WV, USA
[3] UCSD, San Diego, CA, USA
[4] Oak Ridge National Laboratory, Oak Ridge, TN, USA
[5] Princeton Scientific Instruments Inc., Monmouth Junction, NJ, USA
[6] Hiroshima University, Hiroshima, Japan

Received 19 March 2003, accepted for publication 30 October 2003
Published 17 December 2003
Online at stacks.iop.org/NF/44/134 (DOI: 10.1088/0029-5515/44/1/016)

Abstract
The two-dimensional radial vs poloidal structure and motion of edge turbulence in the National Spherical Torus Experiment (NSTX) were measured using high-speed imaging of the visible light emission from a localized neutral gas puff. Edge turbulence images are shown and analysed for Ohmic, L- and H-mode plasma conditions. The two-dimensional images often show regions of strong localized light emission known as 'blobs', which move both poloidally and radially at a typical speed of $\approx 10^5$ cm s^{-1}, and sometimes show spatially periodic features.

PACS numbers: 52.55.Fa, 52.35.Ra

1. Introduction

Turbulence in the edge region of tokamaks and other magnetized plasmas has been measured for many years; however, the theoretical understanding of the experimental observations has been qualitative at best (see [1–4] for reviews). This topic is important to the progress of magnetic fusion since edge plasma conditions will play a significant role in both the plasma–wall interaction and the global plasma performance. During the past few years, powerful three-dimensional computational simulations based on nonlinear fluid models of edge turbulence have become available [5–11], and so it is now possible to make quantitative comparisons of edge turbulence data with such simulations.

This paper presents the first systematic description of edge turbulence in the National Spherical Torus Experiment (NSTX), which is a low-aspect ratio tokamak. These measurements were made using a high-speed camera to produce two-dimensional images of the turbulence structure vs time in the radial vs poloidal plane. A survey of the turbulence observed in various regimes is presented, along with an initial comparison with other types of edge turbulence measurements. Since theoretical simulations of NSTX edge turbulence have not yet been completed, the goal of this paper is to provide experimental data that can help stimulate and eventually test such modelling.

In general, two-dimensional images of edge turbulence in NSTX show the normal turbulent (i.e. random) looking structure in most cases but can also show a variety of coherent (i.e. non-random or intermittent) structure in some cases. As in fluid dynamics, these two-dimensional coherent structures are difficult to characterize or analyse using conventional statistical methods. The significance of these structures can only be understood by comparisons with turbulence theory or simulation, which are beyond the scope of this paper. However, some initial suggestions as to how to make such comparisons are described at the end of this paper.

Previous two-dimensional measurements of edge turbulence were made using Langmuir probe arrays [12–14], thermal lithium beam imaging [15], beam emission spectroscopy (BES) [16] and gas puff imaging (GPI) [17–19]. This paper uses the GPI diagnostic technique, which is described in detail elsewhere [20]. These measurements use an ultra-high-speed camera capable of recording the two-dimensional structure and motion with high space and time resolution in the radial vs poloidal plane. A similar (but lower-resolution) camera was used briefly in Alcator C-Mod [19].

Wide angle images taken using fast cameras in NSTX [17] and MAST [21] have shown that the edge light fluctuations in spherical torus plasmas have a very long (many metres) correlation length along the magnetic field and a short (few centimetres) correlation length across the magnetic field, as

in previous tokamak images made in TFTR [22] and ASDEX [23]. Very long parallel correlation lengths along the magnetic field have also been seen with probes in the scrape-off layer (SOL) in JET [24]. This nearly two-dimensional nature of edge turbulence allows the radial vs poloidal structure to be imaged with GPI by viewing the turbulence from a direction along a magnetic field line.

One generic feature of edge turbulence described in this paper is 'intermittency'. As extensively documented by recent probe measurements in DIII-D [25–27], the edge fluctuations often depart from a Gaussian distribution and feature a significant number of large events above one standard deviation, particularly in the SOL outside the separatrix. This intermittency has been characterized using conditional averaging, with the result that moving, intermittent coherent structures are convected through the edge/SOL of magnetically confined plasmas and can carry a large fraction of the total transport (as discussed in [27] and references therein).

Another generic feature of edge turbulence is its apparent 'universality'. As perhaps first noted by Chen in 1965 [28], the frequency spectrum of turbulence has a similar shape in many types of magnetized plasmas, including various types of gas discharges, linear machines and toroidal fusion devices [29–32]. Some information on the scaling of edge turbulence within and across devices is available [33–35], but a clear identification of the dominant driving and damping mechanisms has not emerged from the data. Not surprisingly, the present results on edge turbulence in NSTX share many features in common with these previous devices.

The outline of this paper is as follows: section 2 reviews the GPI diagnostic, section 3 describes the experimental results and section 4 presents a discussion that includes a comparison with other diagnostics, with experiments and with theory.

2. GPI diagnostic

The GPI diagnostic in NSTX views the edge plasma turbulence in the radial vs poloidal plane near the outer midplane edge of the device. A description of the diagnostic and its interpretation have recently been presented elsewhere [20], and so only a relatively brief description will be presented here.

2.1. Hardware

The GPI diagnostic in NSTX is illustrated in figure 1(*a*). A 30 cm long gas manifold is mounted on the outer wall behind the RF limiter shadow and oriented to produce a cloud of gas extending along the local poloidal direction at the plasma edge. Note that the edge magnetic field lines in NSTX and other spherical tori are inclined at ≈35–55° with respect to the toroidal direction at the outer midplane. The gas puff that leaves this manifold is viewed from a direction nearly along an edge magnetic field line through a re-entrant port about 70 cm away. This view was chosen since edge turbulence is highly correlated along a magnetic field line in NSTX [17] and other machines [22–25], so that the gas puff can localize the light emission to obtain a cross-section of the turbulence in the radial vs poloidal plane.

For these experiments the image of the gas cloud is transferred to a Princeton Scientific Instruments Inc. PSI-4 camera using a lens and mirror inside the re-entrant port

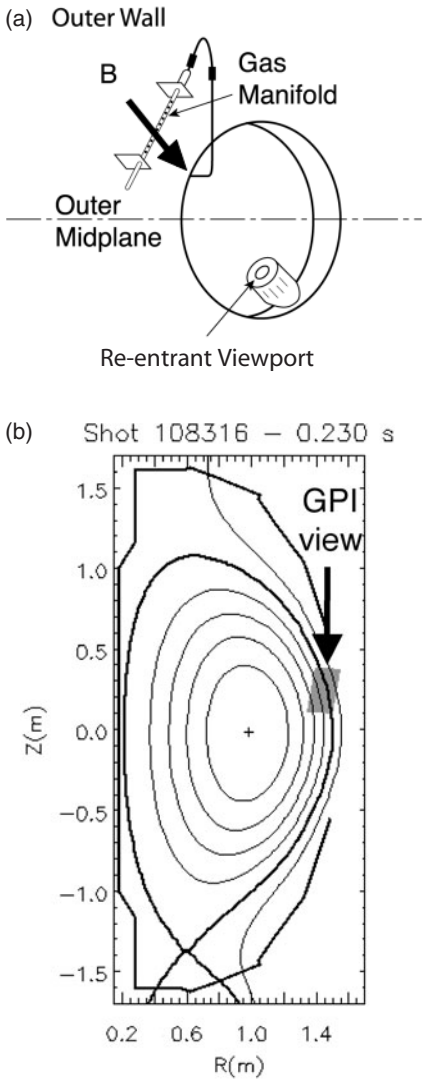

Figure 1. GPI diagnostic geometry in NSTX. In (*a*) is a sketch of the vessel outer wall (as seen from the plasma) showing the re-entrant viewport, the manifold from which the gas puff emerges and the approximate angle of the local magnetic field. In (*b*) is the area of the GPI view indicated by the rectangle just above the outer midplane near the separatrix.

and a 400 × 400 coherent fibre optic bundle. This image is centred near the magnetic separatrix (which is the boundary between open and closed field lines) ≈17° above the outer midplane, as shown in figure 1(*b*). For all the images in this paper, the camera views a ≈32 cm poloidal × 16 cm radial area perpendicular to the magnetic field just inside the gas manifold.

The PSI-4 camera used for these experiments has a specialized CCD that continuously stores the preceding 28 frames on the chip itself. Each frame is made up of 160 × 80 pixels, and framing rates up to 10^6 frames s^{-1} can be obtained. The net quantum efficiency of the CCD is ≈30% in the visible region, the noise level is ≈14 photoelectrons $pixel^{-1}$ with a full-well of ≈25 000 photoelectrons $pixel^{-1}$, and the signals are digitized to 14 bits. The framing rate in NSTX was typically set at 10 μs $frame^{-1}$ to capture turbulent motion with a typical autocorrelation time of ≈40 ± 20 μs. A similar optical system was previously used in NSTX with a 1 kHz framing camera at a 10 μs exposure time [20].

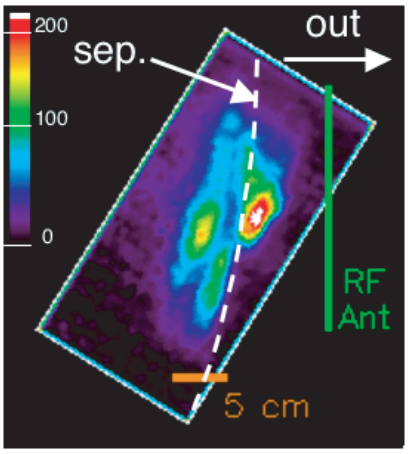

Figure 2. Single image of the He I (587.6 nm) light emission in NSTX as viewed by the PSI camera with an exposure time of 10 μs, oriented so that the local radially outward direction is towards the right (#108609 at 260 μs). The 160 × 80 pixel PSI camera frame indicated by the white rectangle covers an area ≈32 cm × 16 cm in the poloidal vs radial plane. The gas manifold is located ≈3 cm radially outside the toroidal shadow of the RF antenna, which acts as the outboard limiter in these experiments. The intensity scale is indicated by the colour chart at the left, and the magnetic separatrix (as calculated by EFIT) is shown by the dashed white line.

A typical image from the PSI-4 camera is shown in figure 2. This image was made using a He gas puff viewed through a He I optical filter (587.6 nm, 2 nm wide), as were all other images in this paper. Although similar looking images were obtained with a D_2 puff and a deuterium Balmer alpha (D_α) filter, a He puff was normally used in NSTX since the signal/background ratio is larger for He I than for D_α (i.e. without the He puff the images are black on the scale of figure 2). The 160 × 80 pixel camera frame is indicated by the rotated white rectangle, and He I light intensity is displayed using an 8-bit false colour scale (left). The spatial scale and orientation with respect to the local radially outward direction is shown in figure 2 along with the toroidal projection of the RF antenna, which acts as the outer limiter in these experiments, and the magnetic separatrix as calculated by EFIT. The GPI gas manifold is located ≈3 cm radially outside the shadow of the RF limiter at this poloidal location.

The spatial resolution of the optics in this imaging system was ≈0.4 cm over the whole field of view, as measured by the apparent size of a point light source (<0.1 cm diameter) located in the object plane, and was limited by the pixel size (corresponding to 0.2 cm at the gas cloud). However, the spatial resolution of the turbulence structure in the plasma is dominated by the geometrical relationships between the viewing angle, the magnetic field lines and the size of the gas cloud [20]. The typical radial averaging of ≈2 ± 1 cm depends on the radial angle between the sightline and the toroidal extent of the gas cloud, which was measured from a side view using another camera. The poloidal averaging of ≈0.5–2 cm depends on the poloidal angle of the (fixed) sightline with respect to the magnetic field line, which was minimized for the experiments below by optimizing the field line angle. No attempt has yet been made to remove this instrumental spreading from the data since the typical turbulence structure size of ≈4 cm FWHM is significantly larger than the instrumental resolution, although such unfolding could potentially clarify the smallest structures, which presently appear to be ≈1–2 cm FWHM.

For the image presentation in figure 2 (and all other images in this paper) the raw camera data were first normalized to an in-vessel 'white plate' calibration frame to remove optical vignetting and small irregularities in the CCD chip. The data were then digitally smoothed over 3 × 3 pixels (0.6 cm) around each pixel after first replacing each pixel by the median over its surrounding 3 × 3 pixels to remove saturated pixels produced by neutron/gamma noise during neutral beam injection (NBI) discharges. The maximum intensity level seen during the 28 frames for each shot was set to 'white', the zero light level was set to 'black' and the colour scale of figure 2 was applied linearly to the smoothed data. Therefore, these images are simply smoothed versions of the raw camera data vs time.

This image data were supplemented by a set of up to 13 individual detectors for time series analysis. These detectors each viewed a different ≈1.5 cm diameter region of the same image from the camera using an optical beamsplitter. The light from each of these 'chord' data channels was measured by a photomultiplier/preamp with a bandwidth of ≈100 kHz (i.e. 2 μs e-folding time), and these signals were digitized at 500 000 samples s^{-1} for 64 000 samples (0.128 s).

2.2. *Origin of the GPI light emission*

The amount of light emitted in the spectral line in a plasma associated with a radiative transition from neutral atom state p to state q depends on the neutral density and the local electron density and temperature and can be written as

$$S_{pq} = n_0 f_p(n_e, T_e) A_{pq} \qquad (1)$$

where n_0 is the ground state neutral density and A_{pq} is the radiative decay rate of the p to q transition. For GPI, the local n_0 is determined by the neutral gas puff, which is constant over the turbulence timescale (≈2–10 μs) and slowly varying over the turbulence space scale (≈2–10 cm). The function $f_p(n_e, T_e)$ is the ratio of the density of state p to the ground state density. For electron densities and temperatures typical of the edge of fusion plasmas, this ratio is determined by the balance between electron impact excitation, de-excitation, ionization, recombination and radiative decay. Collisional–radiative codes that model this balance for helium have been described by Fujimoto [36] and Goto [37]. The He I (587.6 nm) line used in these experiments results from the 3^3D to 2^3P transition and has $A_{587.6} = 7.1 \times 10^7\ s^{-1}$. Thus, the local light emission rate should follow the local changes in density and temperature due to fluctuations in the frequency range of interest (⩽1 MHz).

The DEGAS 2 neutral transport code [38–40] has been used to estimate n_0 and to calculate the time-averaged light emission expected for He GPI in NSTX, as shown for a typical case in figure 3. The inputs to this code are the edge density and temperature profiles measured by Thomson scattering, shown by smoothed fits at the bottom of figure 3, the magnetic surface geometry as calculated by EFIT, the approximate gas manifold geometry and the effective rates obtained from the He collisional–radiative model [36, 37]. The Monte Carlo routine in the DEGAS 2 code follows neutrals in three dimensions and calculates the He I (587.6 nm) light

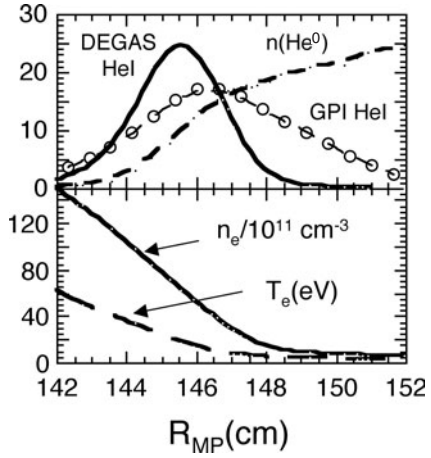

Figure 3. Radial profiles in the edge region of a typical NSTX discharge (#108322) as a function of the major radius along the outer midplane, R_{MP}. The smoothed profiles of n_e and T_e from Thomson scattering are at the bottom, and the calculated profiles of the neutral helium density $n(He^0)$ and He I (587.6 nm) line emission from DEGAS 2 are at the top. The measured GPI He I light emission profile for this shot is shown with circles in the top part. The separatrix is approximately at $R_{MP} = 148.5 \pm 1$ cm in this case.

emission. This simulation assumes toroidal symmetry and does not replicate the experimental camera view. Instead, the simulation results are presented as plots in the radial–poloidal plane. The peak of the calculated He I emission occurs at $T_e \approx 20$ eV, and agrees with the measured time-averaged He I emission for the same discharge (#108322) to within ≈1 cm, as shown in figure 3. However, the width of the calculated emission is significantly narrower than the measured emission, most likely due to the simplified geometry in DEGAS 2 and/or to the effect of turbulence on the light emission. A similar level of agreement was obtained between DEGAS 2 and the D_α light emission profile during GPI in Alcator C-Mod [19, 39].

According to equation (1), local fluctuations in He I light emission S could be due to fluctuations in n_e, T_e or n_0. The dependence of $S_{587.6}$ on n_e and T_e near the centre of the emission cloud dependence is roughly $S \propto n_e^{0.5} T_e^{0.7}$, but these exponents vary with n_e and T_e (see section 4.1). The interpretation is somewhat simplified if the electron density and temperature fluctuations are in phase, as expected theoretically and approximately verified using Langmuir probes in DIII-D [26] and TEXT [41]. However, even then it is difficult to unfold directly the density fluctuations from the light emission fluctuations when the n_e and T_e fluctuations are large.

The possible influence of a varying neutral density caused by the turbulence itself was discussed in [39] for deuterium GPI in Alcator C-Mod, and the situation should be similar for He in NSTX. For example, a large positive density or temperature perturbation could ionize some of the He neutrals and lead to a decrease in the neutral density and He I light emission radially inside this perturbation (i.e. 'shadowing'), somewhat similar to the 'edge' effect seen in BES measurements [16]. This has been simulated using DEGAS 2 with simplified models for density and temperature perturbations. The spatial structure of the resulting He I light fluctuation patterns has so far been found to be close to the structure of the assumed density or temperature perturbations (although the relative fluctuation levels are different). Experimentally, the shadowing effect would produce a radial dipole-type structure in which a high density at larger radius would be correlated with a small density at smaller radius and vice versa. However, there is little or no sign of such shadowing in either the image data or the chord data.

In this paper, the experimental results will be presented and analysed in terms of the He I light emission itself without attempting to unfold the underlying density or temperature fluctuations. However, the space–time structure of the turbulence seen in these images should be similar to the structure of the underlying plasma turbulence, on the basis of numerical simulations (section 4.1) and comparisons with other edge turbulence diagnostics (section 4.2). For a more quantitative comparison between theory and simulation, an atomic physics/neutral model such as DEGAS 2 can be used as a 'post-processor' to calculate the expected GPI images from the turbulence model results, thus avoiding the need to unfold directly the temperature and density fluctuations from the GPI data. This procedure has been done with some success for GPI data from Alcator C-Mod [19] and will be done for NSTX when theoretical simulations become available.

2.3. Experimental limitations and uncertainties

A major limitation in these results is the relatively small range of space and time covered by the present GPI diagnostic. In particular, He I emission occurs only where the electron temperature $T_e \approx 5$–50 eV, which corresponds to a radial range of only 3–8 cm (FWHM) in NSTX. This turns out to be ≈1–2 radial correlation lengths, thus making it difficult to determine the radial k-spectrum. The poloidal resolution of this system is presently limited to ≈1 cm by GPI geometry (for optimum viewing angles), thus limiting the k-resolution to the region $\leqslant 4\ \mathrm{cm}^{-1}$. The framing rate and duration of the imaging were also constrained by the number of camera frames per shot (28), which made it difficult to evaluate the time evolution during a discharge. The usual frame integration time of 10 μs was chosen to minimize blurring of fast moving features yet allow the motion to be seen over several autocorrelation times.

A major uncertainty in this data is the location of the magnetic separatrix with respect to the GPI imaging area. Modelling based on the SOL power balance in NSTX [42] suggests that the separatrix electron temperature should be roughly ≈20–50 eV for the L- and H-mode cases and ≈10–30 eV for the Ohmic cases, depending on input assumptions. However, the separatrix determined by EFIT is presently located in regions where $T_e \approx$ 10–20 eV (see section 3.1), which for H-mode plasmas is ≈1–2 cm farther out than expected from power balance. This discrepancy is not yet resolved. In addition, for the discharges of table 1, the angle of the calculated separatrix in the plane of the GPI image was ≈10° off from the angle of the narrow GPI light emission cloud during H-modes, probably due to an angular misalignment of the GPI optics during this part of the run. However, on the basis of DEGAS 2 simulations [40] and other results during the later part of the run, it was assumed for these cases that the time-averaged light emission was constant along a local magnetic flux surface, which then defined the local poloidal direction (see section 3.1).

Table 1. Shot list (all 10 μs gating, He puff with He I filter).

Shot #	t (ms)	B (kG)	I (kA)	$\langle n_e \rangle^a$	P (MW)	Type
108164	240	3.0	800	3.0	0	Ohmic
108243	298	4.5	950	3.7	1.7	L-mode
108289	200	3.0	800	2.5	0	Ohmic
108290	200	3.0	800	2.5	0	Ohmic
108291	200	3.0	800	2.1	0	Ohmic
108292	180	3.0	780	3.0	0	Ohmic
108293	180	3.0	770	3.2	0	Ohmic
108294	230	3.0	750	4.5	0	Ohmic
108295	210	3.0	800	3.9	0	Ohmic
108296	220	3.0	780	4.2	0	Ohmic
108297	200	3.0	780	3.5	0	Ohmic
108300	180	3.0	780	1.9	0	Ohmic
108301	180	3.0	750	3.0	0	Ohmic
108302	240	3.0	740	4.4	0	Ohmic
108303	240	3.0	750	3.1	0	Ohmic
108309	250	4.5	890	3.1	1.7	L-mode
108310	250	4.5	890	3.0	1.7	L-mode
108311	270	4.5	890	3.9	1.7	H-mode
108313	270	4.5	900	3.0	1.7	L-mode
108314	230	4.5	900	3.2	1.7	H-mode
108315	230	4.5	900	3.3	1.7	L-mode
108316	230	3.5	890	2.9	1.7	H-mode
108317	230	3.5	900	2.9	1.7	H-mode
108320	180	3.5	940	2.0	1.7	L-mode
108321	180	3.5	900	2.1	1.7	L-mode
108322	180	3.5	920	2.0	1.7	L-mode

[a] Line-averaged density ($\times 10^{+13}$ cm^{-3}).

As described before, a general limitation in these results is the uncertain relationship between density and temperature fluctuations, both of which can contribute to fluctuations in the measured He I light emission. However, if these fluctuations are correlated, as expected for turbulent fluid motion dominated by $E \times B$ advection with negligible magnetic flutter, then the resulting structure of the He I light emission should be similar to both (see section 4.1).

Another uncertainty in the interpretation of the He I light emission is the possible effect of metastable states on the emission. These metastable states are included in the basic atomic physics model of DEGAS 2 but only assuming that they equilibrate on a transport timescale. However, preliminary results from DEGAS 2 made by treating the metastables separately (without this assumption) are not significantly different. Also, since images in D_α look similar to He I (587.6 nm) images (see section 3.4), this detail of the He atomic physics is unlikely to be an important effect.

The gas puff used for imaging the turbulence in these GPI measurements does not perturb significantly either the plasma edge or the edge turbulence itself, as discussed previously [20]. The evidence for the lack of a perturbing effect is the following: (a) the insensitivity of the turbulence with respect to the strength of the He gas puff seen in the GPI diagnostic itself (section 3.2), (b) the similarity of the turbulence seen in GPI measurements with either He or D_2 puffs (section 3.4), (c) the similarity between the turbulence spectra seen in other edge diagnostics and the GPI spectra (see section 4.2), (d) the insensitivity of the turbulence measured by other edge diagnostics to the presence or absence of the GPI He puff (section 4.2) and (e) the absence of a significant change in edge plasma parameters associated with the gas puff. The maximum GPI He puff rate was $\approx 6 \times 10^{20}$ atoms s^{-1}, corresponding to $\approx$1 Torr l entering over a time of $\approx$0.1 s (see figure 4), which is much smaller than used for normal gas fuelling in NSTX (typically 20 Torr l of D_2 in 0.1 s) and very much smaller than the $\approx 10^{22}$ atoms s^{-1} in the strong puffing case analysed for TEXTOR [43]. The absence of a perturbing effect of the gas puff on the edge turbulence is similar to that observed previously in PBX-M [44].

3. Experimental results

This section describes the measurements and analysis of the space vs time patterns of the He I light emission seen with GPI in NSTX. Typical image data and image analysis are presented in section 3.1, time series data and analysis from the discrete 'chord' detectors are presented in section 3.2, discussion of possible coherent structures is presented in section 3.3 and other imaging results are described in section 3.4. The relationship between the light emission fluctuations and the underlying density and temperature fluctuations is discussed in section 4.1.

Figure 4 illustrates time dependences for a typical NSTX discharge, where $R = 90$ cm, $a = 65$ cm, $B = 3.5$ kG, $I = 850$ kA and 1.7 MW of NBI, for 0.08–0.45 s (#108980). Other global parameters for this shot are $\kappa \approx 1.8$, $q(a) \approx 8$, $\tau_E \approx 30$ ms and $\beta_T = 10\%$. The plasma current and line-averaged density are approximately constant over 0.2–0.35 ms, as shown in the top two traces. The He puff for GPI starts at 0.27 s, and the PSI camera was triggered at 0.29 s in this shot.

3.1. Image data

A list of the NSTX discharges used for image analysis in this paper along with their global parameters is shown in table 1. Most of these were taken on the same day (5/13/02). Many of these discharges had NBI, and none had high-harmonic fast wave heating. Typical parameters for one of these discharges are listed in table 2, and a typical equilibrium is shown in figure 1.

Three examples of high-speed images of He I light emission in NSTX are shown in figure 5 (animations can be seen on the Web site http://www.pppl.gov/∼szweben). These particular images are for (*a*) an Ohmic discharge, (*b*) an L-mode discharge and (*c*) a quiescent H-mode discharge. In each case, there are ten successive frames taken at 10 μs frame^{-1} with the same field of view and image processing as for figure 2 (see section 2.1). However, the images in figure 5 are not rotated (for compactness) and so the radially outward direction is towards the upper right, as shown by the arrow in the first frame of figure 5(*c*). For the image analysis below, it was assumed that the local poloidal direction was along the line of constant He I emission in figure 5(*c*), but small uncertainties in this angle do not change the results significantly (see below).

The Ohmic discharge in figure 5(*a*) shows the normal behaviour of these images, which largely consist of bright $\approx$4 cm FWHM emission regions that change shape and size as they move across the field of view within $\approx$50–100 μs (5–10 frames). The L-mode discharge in figure 5(*b*) has similar features, but the emission pattern is somewhat narrower in the radial direction. The H-mode case in figure 5(*c*) was captured

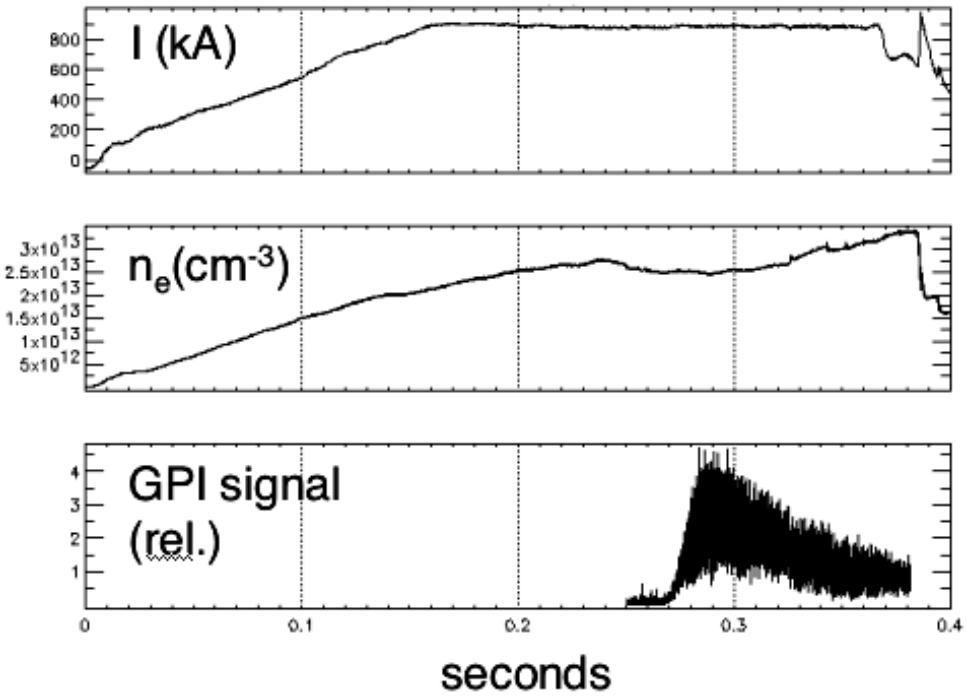

Figure 4. Time evolution of a typical discharge in NSTX (#108980). At the top is the plasma current, in the middle is the line-average plasma density and at the bottom is the He I light emission from the GPI He gas puff. The He gas puff enters the plasma at 0.27 s, and the fast image capture was at 0.2900–0.290 28 s.

Table 2. Typical NSTX parameters.

Shot #108322 at 0.18 s
$B(0) = 3.5$ kG (on axis)
$I = 900$ kA
$T_e(0) = 1$ keV
$n_e(0) = 2.5 \times 10^{13}$ cm^{-3}
$\langle n_e \rangle = 2 \times 10^{13}$ cm^{-3} (line averaged)
Outer edge ($R_{MP} = 146$ cm)
$n_e \approx 5 \times 10^{12}$ cm^{-3}
$T_e \approx 13$ eV
$\beta \approx 10^{-3}$
$L_n \approx 2$ cm
$\rho_s \approx 0.2$ cm
$\nu_{ei} \approx 6 \times 10^6$ s^{-1}
$L_c \approx 5$ m[a]
$\lambda_{ei}/L_c \approx 0.05$
q (local) $= (B_T/B_{pol})(R/a) \approx 2$
$L_{RBM} \approx 1$ cm[b]

[a] Connection length to divertor.

[b] RBM scale.

during a very quiescent period and has a narrow and nearly constant emission region; other H-mode images are not so quiescent (see sections 3.2 and 3.3).

An analysis of the images from these three discharges is shown in figure 6. For this figure, the images were first rotated to the radial vs poloidal direction (as for figure 1) and then sliced into boxes 0.6 cm radially × 18 cm in the poloidal direction. At the top of figure 6 are the time-averaged He I intensity profiles 'I', averaged over the poloidal length of each box and over all 28 frames for that shot (figure 5(a) shows the analysis region). In the next row are the relative fluctuation levels, '$\delta I/I$', derived as follows: first, each two-dimensional frame is normalized by the time-average over all 28 frames in that shot to minimize the effects of the finite size of the He gas cloud; second, the rms deviations within each poloidal box from its average are calculated for each frame; and third, these rms deviations for each box are averaged over all 28 frames of the shot. In the next row are the poloidal correlation lengths, L_{pol}, derived as follows: first, each individual frame is normalized by the time-average over all 28 frames to minimize the effects of the finite size of the He gas cloud; second, the un-normalized poloidal cross-correlation functions (i.e. covariances) are calculated for each box for each frame; third, these covariances are summed for each box over all 28 frames; and fourth, the FWHM of the resulting poloidal cross-correlation function is defined at L_{pol} for that box. At the bottom are the density and temperature data from the Thomson scattering diagnostic for these shots at a time within ≈1 ms of the GPI image data.

The average He I light emission peaks near $T_e \approx 10$–20 eV in each case, approximately as expected from the DEGAS 2 modelling (figure 3). The radial width of this emission is approximately 8 cm FWHM for the Ohmic case, 6 cm for the L-mode case and 3 cm for the H-mode case. This width is most likely determined by the electron temperature and density profiles, which determine the local excitation rates, which in turn are determined by the edge plasma profiles in a particular discharge. Roughly speaking, the He I emission covers the region where $T_e \approx 5$–50 eV in NSTX. The locations of the last closed flux surfaces (LCFS) are indicated at the top, each with estimated uncertainties of 1–2 cm. The L- and H-mode plasmas are lower single-null diverted, while the Ohmic plasma is limited on the inner wall.

The relative He I fluctuation levels for the Ohmic and L-mode plasmas were in the range ≈10–60% and increased

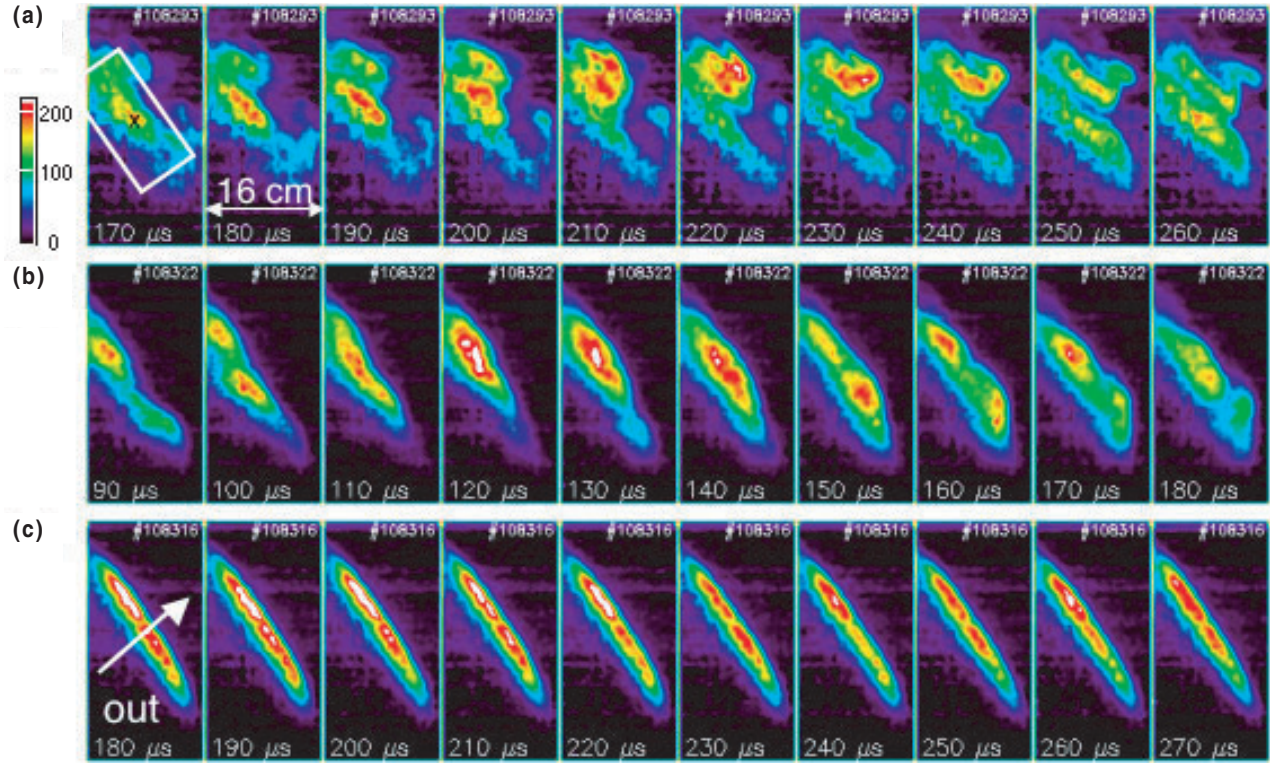

Figure 5. Typical time sequences of images from NSTX taken in He I light with the PSI camera at 10 μs frame^{-1}, here showing ten of the 28 frames per shot. These images cover the same area as the tilted rectangle in figure 2 and have the same colour scale but are oriented with the radially outward direction towards the upper right (see arrow in the left bottom panel). Case (*a*) is an Ohmic discharge (#108293), case (*b*) is an L-mode (#108322) and case (*c*) is a quiescent H-mode (#108316). The area used for image analysis is shown in the upper left frame.

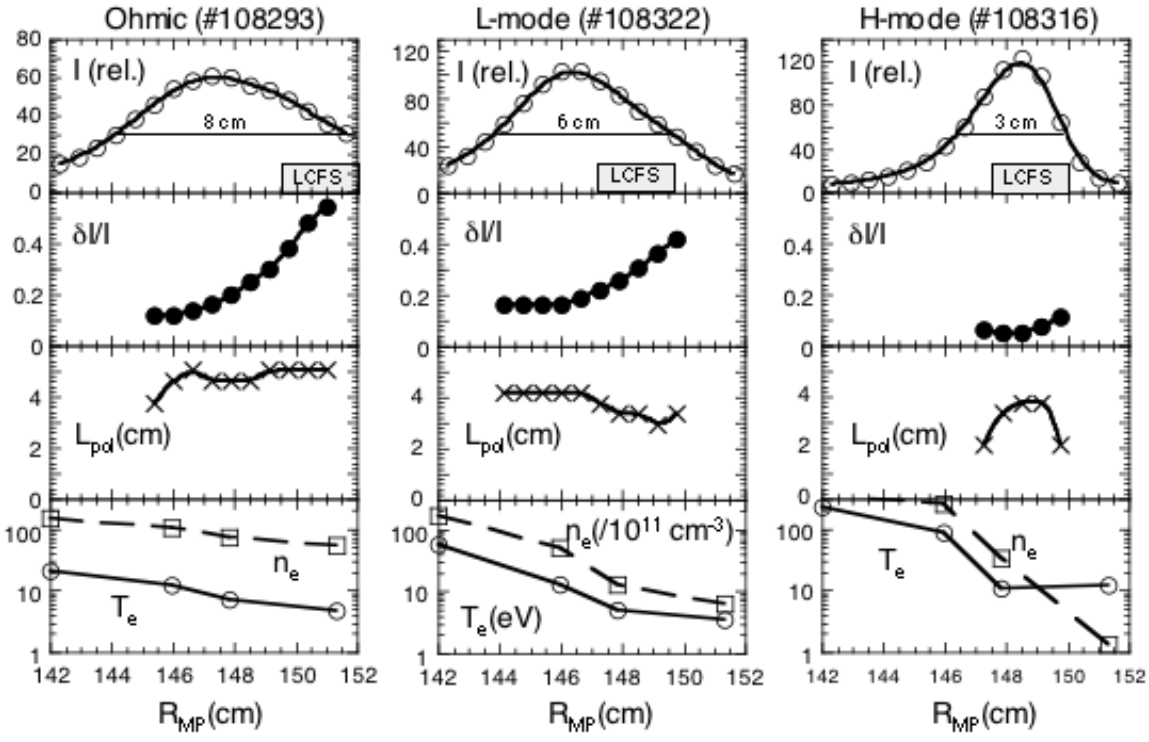

Figure 6. Time-averaged radial profiles of the He I light intensity, I (top), its relative fluctuation level, $\delta I/I$, the poloidal correlation length of the fluctuations, $L_{\rm pol}$, and the Thomson scattering data for $n_{\rm e}$ and $T_{\rm e}$ for the three discharges of figure 5. The first three quantities are averaged over the 28 frames in the PSI camera data for each of these shots. The approximate separatrix locations are shown at the top.

monotonically towards the wall. The fluctuation level in this particular H-mode image sequence was only 5–10% at the centre of the relatively narrow He I emission cloud. The poloidal correlation lengths, L_{pol}, as shown in the third row of figure 5 were typically 4 ± 1 cm and approximately constant vs radius in the region of brightest He I emission. The correlation lengths appear to decrease away from the brightest region of the H-mode case, but this may be due to the relatively low signal/noise level for these small fluctuation levels.

Figure 7 shows the relationship between L_{pol} and $\delta I/I$ for a larger set of discharges (see table 1), as evaluated near the radial peak of the He I emission cloud for each case. Some H-mode shots have fluctuation levels comparable with Ohmic shots; other H-mode cases (not shown) had fluctuation levels below 5%, at which point evaluation of L_{pol} was difficult. In general, the poloidal correlation lengths were in the range $L_{pol} \approx 4 \pm 1$ cm, with no obvious variation among discharge types, and the relative fluctuation levels were lower on average in H-mode plasmas than in Ohmic or L-mode plasmas.

Figure 8 illustrates the poloidal k-spectral amplitude for the three cases of figures 5 and 6. These spectra were obtained from FFTs of the poloidal spatial distributions near the radial peak of the He I emission cloud after normalizing each frame as a whole to the time-averaged frame for each discharge. The shapes of these three k-spectra are similar, but with the H-mode case having a significantly lower total fluctuation level. Note that these k-spectra have not been corrected for the poloidal spatial resolution of ≈1 cm expected for these cases (see section 2.1). Thus the k-spectra of figure 8 systematically underestimate the amplitudes above $k_{pol} \approx 2$–$4\,\mathrm{cm}^{-1}$, and so the main result of figure 8 is just that the k-spectra have a width of $\Delta k \approx 1\,\mathrm{cm}^{-1}$ in the poloidal direction.

Figure 9 shows the time-averaged correlation lengths as a function of the angle in the radial vs poloidal plane for a set of typical Ohmic and L-mode discharges. In each case this L (cm) is the FWHM of the correlation function calculated in a 0.6 cm wide × 12 cm long box rotated about the point 'x' shown at the left of figure 5(*a*) after normalizing by the time-averaged frame in each case. There is a trend for the radial correlation lengths to be slightly shorter than the poloidal correlation lengths but not much more than by the frame-to-frame variation within a single shot (shown by the error bars). Thus, the turbulence is approximately isotropic in the radial/poloidal plane in these cases. The emission clouds for H-mode plasmas are too narrow in radius for the angular variation to be estimated this way.

The dependence of edge turbulence on plasma density during the Ohmic discharges of table 1 is shown in figure 10. Here, the relative fluctuation levels and poloidal correlation lengths are plotted near the radial peak, R_{peak}, of the He I

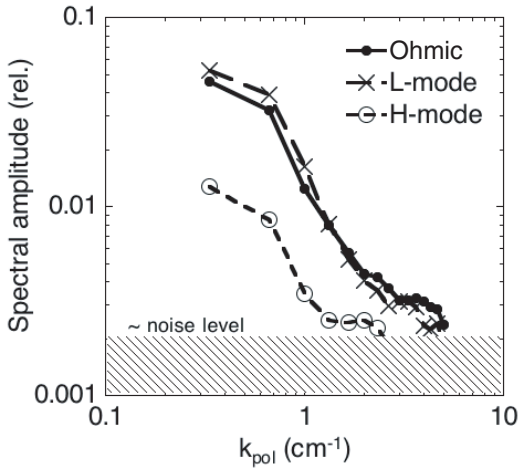

Figure 8. Time-averaged poloidal k-spectra for the shots of figure 5 as evaluated using the PSI images near the radial peak of the He I emission. There is no significant difference between the shape of the k-spectra between these three cases, but the fluctuation level is lower in this relatively quiescent H-mode case.

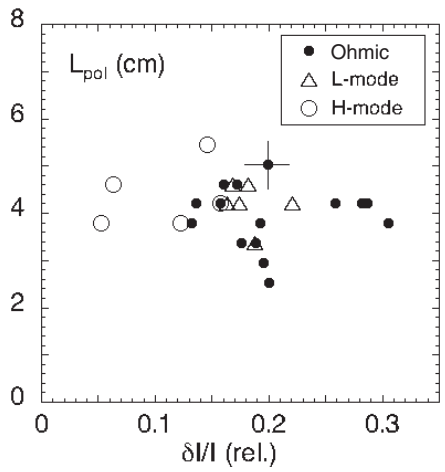

Figure 7. Relationship between the poloidal correlation lengths, L_{pol}, and $\delta I/I$ for the shots in table 1 as evaluated near the radial peak of the He I emission and averaged over the 28 frames of PSI data for each shot. The error bars represent typical rms variations from frame-to-frame within each shot. There is no significant variation in the average L_{pol} between Ohmic, L- and H-mode cases in these data, but the H-mode cases tend to have a lower fluctuation level.

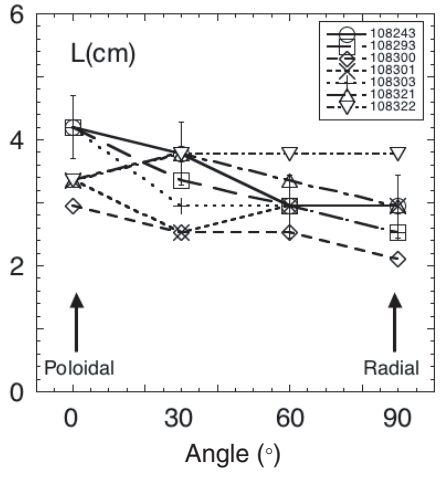

Figure 9. Correlation lengths of the turbulence as a function of the orientation angle in the poloidal vs radial plane. The analysis was done by rotating the images around the point labelled with an 'x' within the analysis box shown in the first image of figure 5(*a*). The correlation length in the radial direction is slightly smaller than in the poloidal direction (error bars show frame-to-frame variation within a shot). These discharges are Ohmic and L-mode cases from table 1 (#108243, 321 and 322 are L-mode, and the others are Ohmic).

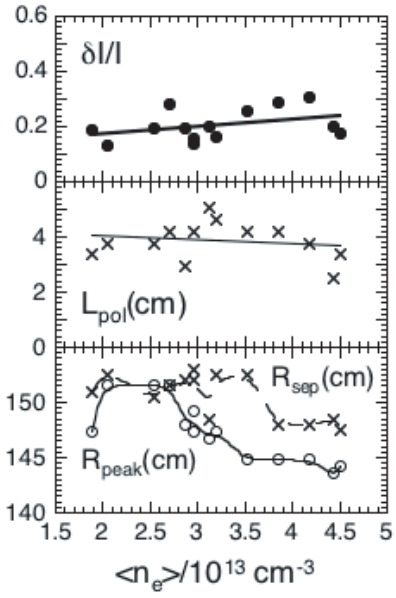

Figure 10. Variation of the poloidal correlation length and relative fluctuation levels during an Ohmic density scan at constant current and field ($B = 3$ kG, $I = 750$–800 kA). The horizontal variable is the line-averaged density, and each point is the average over the 28 frames in the PSI data evaluated near the radial peak of the He I light emission. There is little or no significant variation in the turbulence observed over this range, which extends up to 0.8 times the Greenwald density limit. However, the peak of the He I light emission shifts outwards at a lower density, in part due to an inward shift of the separatrix.

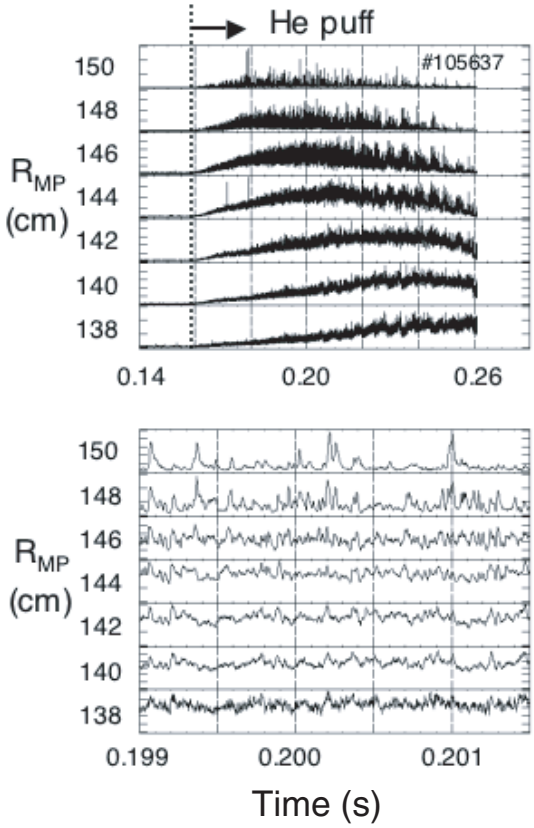

Figure 11. Typical signals from the radial array of fast GPI chords that viewed small regions of the He I light image seen by the PSI camera. Each chord views an ≈1.5 cm diameter area near the poloidal centroid of the He I light emission cloud. The top plot shows the He gas puff entering the discharge at 0.16 s, and the bottom plot shows an expanded timescale of the top plot. The separatrix was approximately at a midplane major radius of $R_{MP} = 150$ cm for this Ohmic shot (#105637). The vertical axes depend upon the local neutral density and so are different for each radial channel.

emission cloud as a function of the line-averaged density, $\langle n_e \rangle$. There was no significant change in $\delta I/I$ or L_{pol} with density in this range, which goes up to ≈0.8 times the Greenwald density [45]. There is, however, a general shift of the radial peak of this emission to smaller major radius as the density increases, as shown at the bottom of the figure, which is partly due to an inward shift of the separatrix, R_{sep}, at higher density and probably also to a decrease in edge temperature with increasing density. Since it is not yet clear whether NSTX has a density limit consistent with the Greenwald scaling, these measurements cannot yet be compared with edge fluctuation measurements near the density limit in other devices.

3.2. Time series data

As described in section 2.1, the image could be optically split and sent to a set of discrete fibres, each of which viewed a ≈1.5 cm diameter area at the He I emission cloud in the plasma. Since these chords sample a region much smaller than a correlation length, they can be used for time series analysis of the local turbulence properties.

Typical results from a radial array of seven chords each separated by 2 cm near the poloidal centroid of the He I emission cloud are shown in figure 11. The He puff begins at ≈0.16 s in this case, which was an Ohmic plasma with $B = 3$ kG and $I = 700$ kA (similar to the Ohmic cases of table 1). The slow-time evolution is shown at the top, and a fast timescale for part of these signals is shown at the bottom. The location of each chord is specified by the major radius of its magnetic flux surface as measured along the outer midplane, i.e. R_{MP}. The separatrix for this shot is at $R_{MP} \approx 149 \pm 1$ cm, i.e. most of these chords are inside the separatrix.

The radial profile of the relative fluctuation level, $\delta I/I$, for this case is shown in figure 12. This profile shows $\delta I/I$ increasing from ≈10% inside the separatrix to ≈90% outside the separatrix, which is qualitatively similar to the image analysis for the Ohmic case in figure 6 (the slightly larger fluctuation levels at the outer edge of figure 12 are most likely due to small differences between these two discharges). Also illustrated in figure 12 is the similarity of the radial profiles of $\delta I/I$ just after the start of the He gas puff (0.165 s) and near its peak (0.2 s), showing that the GPI signals are insensitive to at least a factor of 4 change in the He flow rate [20]. The radial fluctuation profiles seen in this chord array for L- and H-mode plasmas are also qualitatively similar to those in the image analysis of figure 6.

A time series analysis of two chords from the same Ohmic discharge is shown in figure 13. This analysis uses 10 000 time points between 0.19 and 0.21 s for one of the outer channels ($R = 150$ cm) and an inner channel ($R = 144$ cm). Both chords show short autocorrelation times of $\tau_A \approx 32$ and 24 μs (τ_A is defined as the HWHM of the autocorrelation function),

with no longer-time correlations visible. The power spectra are nearly flat below between ≈0.1 and ≈10 kHz, except for some MHD modes (these spectra have been corrected for the amplifier frequency response). The probability distribution functions (PDFs) have a Gaussian shape when the relative fluctuation level is $\delta I/I \leqslant 20\%$ (e.g. at 144 cm) and a non-Gaussian shape where the relative fluctuation level is $\delta I/I \geqslant 50\%$ (e.g. at 150 cm). Such non-Gaussian or 'intermittent' PDFs are common in edge turbulence (see section 4.3), especially at large relative fluctuation levels, in part since the signal itself can never go negative. Higher-order moments of these time series such as skewness and kurtosis could also be calculated from these signals, but their quantitative interpretation may depend upon the sensitivity of the light emission to the local density and temperature (see section 4.1). The autocorrelation times, frequency spectra and PDFs in H- and L-mode plasmas were roughly similar to those for Ohmic plasmas.

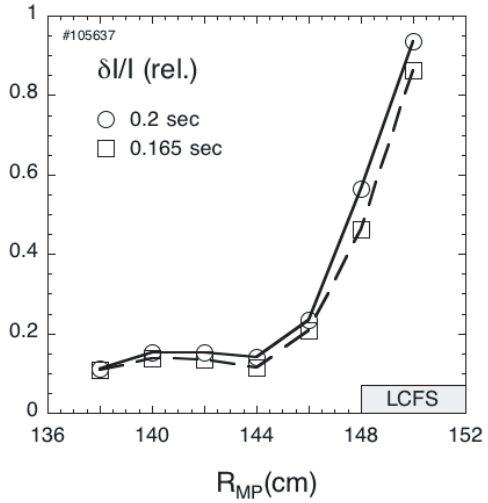

Figure 12. Radial profile of the relative fluctuation level, $\delta I/I$, seen by the discrete chord array for the same Ohmic discharge as in figure 11. As expected, the profile shape is similar to the image data for the (slightly different) Ohmic discharge in figure 6. The fluctuation level is very similar just after the start of the He puff (0.165 s) and at the peak of the He puff (0.2 s), over which time the He puff rate varies by about a factor of 4.

The most interesting information in the time-dependent chord signals concerns the transition from H- to L-modes and vice versa since there are (so far) no PSI camera images that have captured these transitions. An example of the variation of the radial array signals during an H–L transition is shown in figure 14. The He gas enters during the H-mode phase at 0.18 s, and the H–L transition occurs at ≈0.215 s in this case. The transition was correlated with a large pulse of He I light that propagates outwards across this array at a speed of $\approx 10^6$ cm s^{-1}, as shown in the bottom of figure 14. This pulse occurs over a very short timescale of ≈30 μs, which is comparable with the autocorrelation time of the L-mode turbulence. There is also a growing oscillation in the middle channel just before this pulse, which may be a trigger to this event. It is likely that edge profile changes are also occurring over this timescale, and so it is difficult to interpret these changes quantitatively. Only a few cases of this type have been captured so far, and so is not clear that this is a universal feature of the H–L transition.

An example of the GPI chord signals during an L–H transition is shown in figure 15, where the He gas enters at 0.39 s and the H-mode transition is at 0.403 s. For the chords

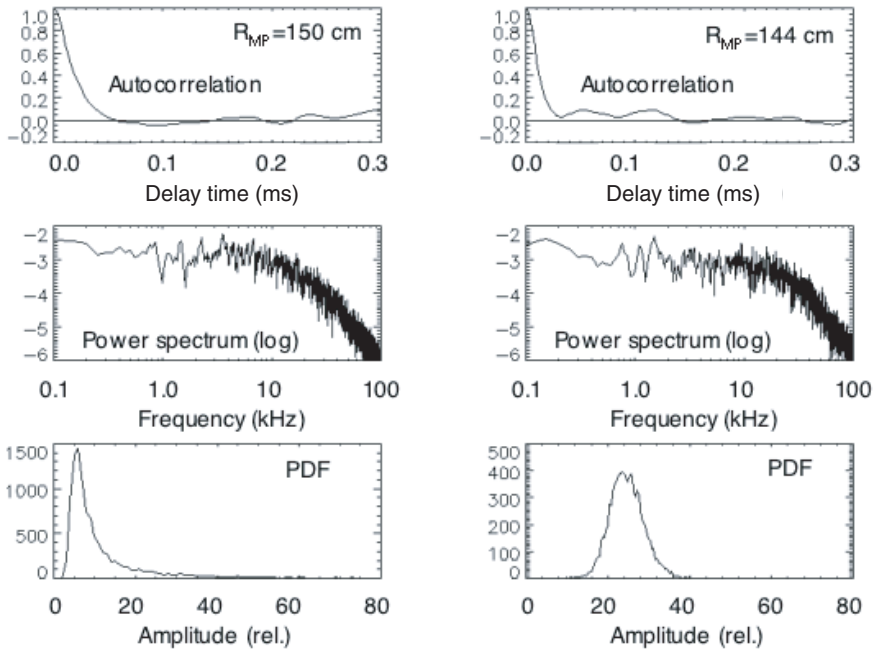

Figure 13. Time series analysis of the He I emission fluctuations in the radial array of chords shown in figure 10. At the left is the chord at $R_{MP} = 150$ cm and at the right is the chord at $R_{MP} = 144$ cm, and both analyses are done with 10 000 time points (0.19–0.21 s). The autocorrelation times are 32 μs and 24 μs FWHM, respectively, and the power spectra show a flat region between 0.1 and 10 kHz (except for some MHD near 1 kHz) and a decrease in power of ⩾100 between 10 and 100 kHz. The signal levels without a He puff are below '−6' on this power scale. The PDFs are non-Gaussian in the outermost channel and Gaussian in the inner channel.

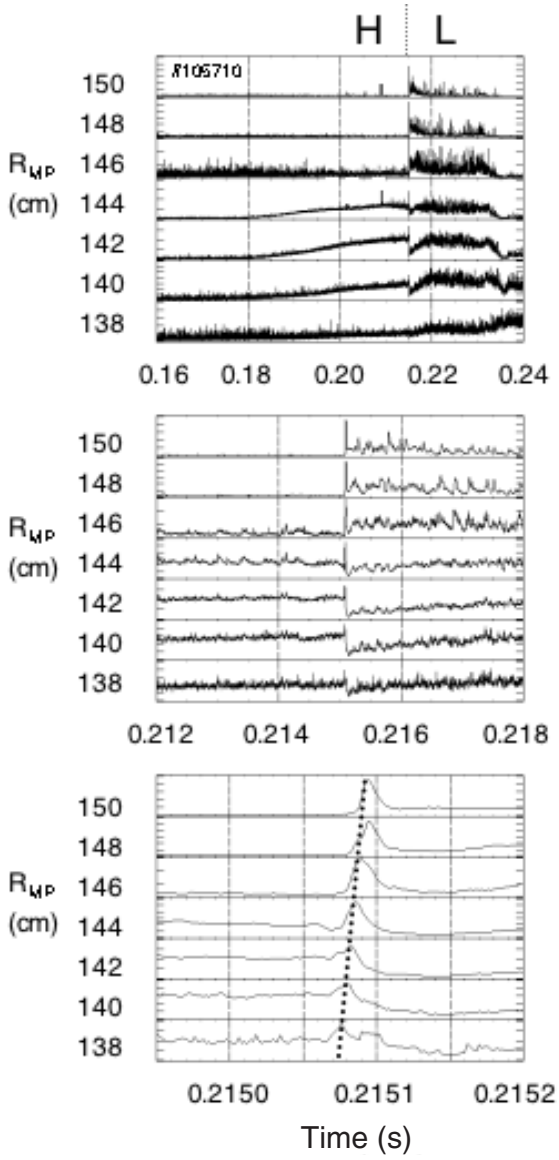

Figure 14. Time dependence of the He I light emission during an H–L transition as seen in the radial array of fast GPI chords. The He puff enters at 0.18 s, and the three panels show successive close-ups around the H–L transition at 0.215 s. During the H-mode, the emission is localized in the chords at $R_{MP} = 140$–144 cm, while during the L-mode the radial profile is broader (as seen in figures 5 and 6). There is a $\approx 30\ \mu$s long pulse propagating out towards the separatrix just at the H–L transition in this case (#105710), where the separatrix is at $R_{MP} \approx 150$ cm. The vertical axes depend upon the local neutral density and so are different for each radial channel.

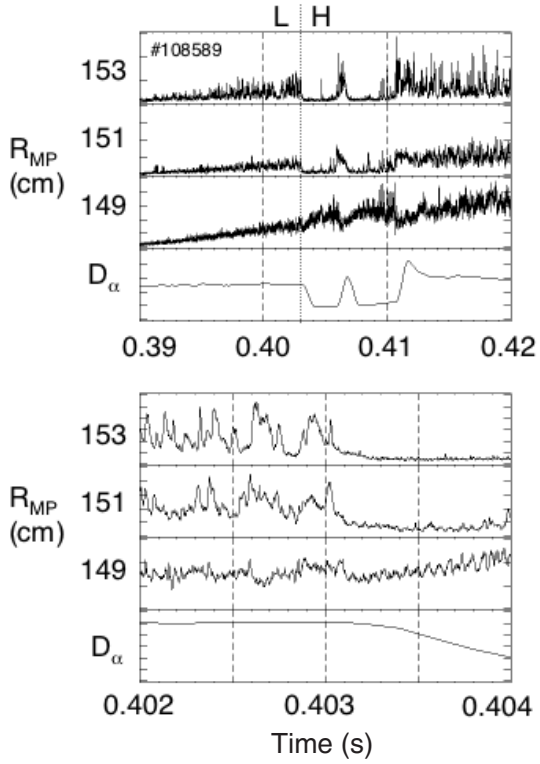

Figure 15. Time dependence of the signals during an L–H transition as seen in three of the fast GPI chords. The transition occurs at ≈ 0.403 s in this shot (#108589), as measured by the drop in D_α light in the bottom traces (the D_α signal has a frequency response of only ≈ 2 kHz). The GPI signal levels in the outer two chords at $R_{MP} = 153$ and 151 cm drop within $\approx 100\ \mu$s at the H-mode transition with no obvious precursors. An apparently unrelated ≈ 20 kHz MHD mode is visible in the inner channel during the H-mode phase in this discharge. The vertical axes depend upon the local neutral density and so are different for each radial channel.

at $R_{MP} = 153$ and 151 cm, the average brightness decreases within $\approx 100\ \mu$s after the transition, corresponding to the region where He I is not emitted during the H-mode (see figure 5), and at $R_{MP} = 149$ cm the average brightness increases at the H-mode transition, corresponding to the region where the He I light is bright during the H-mode. There are no obvious precursors to the H-mode transition in this or the few other cases seen so far. Most of the fluctuations after the H-mode onset in the chord at $R_{MP} = 149$ cm are correlated with a coherent mode seen on the Mirnov signals at ≈ 20 kHz and are unlikely to be related to the H-mode transition (see section 3.3).

Finally, during H-modes, there are often edge localized modes (ELMs) of varying sizes that appear as transient increases in the D_α emission [46]. Examples of GPI He I chord light signals during an H-mode with large ELMs are shown in figure 16. Most of the fluctuations seen in the GPI chords appear as intermittent bursts largely independent of the relatively slow D_α ELM events. The GPI bursts (particularly in the outermost channels) last $\approx 100\ \mu$s and often (but not always) propagate outwards at $\approx 10^5$ cm s^{-1}; thus, they have a spatial and temporal structure similar to the 'blobs' seen in the imaging system, especially during H-modes (section 3.3). There is some correlation of the large ELMs with an increase in the GPI burst amplitude in the outermost channel, probably due to an increase in edge density due to the ELM. It is possible that there are small, localized and/or fast D_α bursts similar to the GPI bursts that are not resolved by the present D_α detectors, which have a frequency response of only ≈ 2 kHz and are located far from the GPI viewing region.

3.3. Coherent structure and motion

One of the motivations for imaging plasma turbulence is to search for 'coherent structures', which may roughly be defined as self-organized and relatively long-lived structures

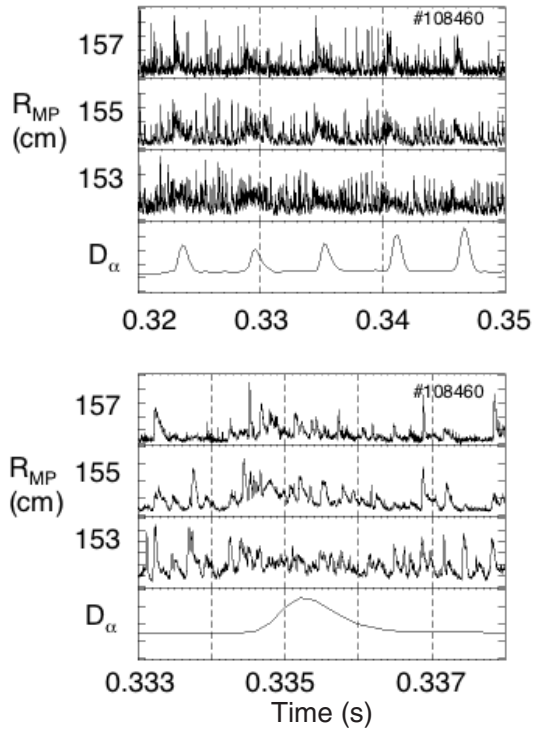

Figure 16. Time dependence of the GPI fast chord signals during ELMs in an H-mode shot (#108460). Between the ELMs, which are coincident with the rise in D_α light in the bottom traces, there is an intermittent or bursty turbulence in the outer GPI channels similar to that seen in Ohmic discharges (figure 11). During the ELMs, there is only a modest change in this bursty turbulence, e.g. an increase in the amplitude of the bursts outside the separatrix (which was at $R_{MP} \approx 153 \pm 1$ cm in this case). The vertical axes depend upon the local neutral density and so are different for each radial channel.

that exist within fully developed turbulence. In neutral fluids, coherent structures are often seen as vortices, e.g. in near-wall turbulence [47], but they can have many different forms such as 'bubbles', 'spikes', 'mushrooms', 'fingers', 'hairpins', 'jets', 'rings', etc [48]. Such structures are generally difficult to detect with single-point measurements except by statistical techniques such as conditional sampling, which average over many events. Examples of such non-random structures within tokamak turbulence include 'blobs' (sometimes called 'intermittent plasma objects (IPOs)') [25–27, 29, 32, 49], quasi-coherent modes [50], zonal flows [51] and perhaps avalanches [52].

Some examples of localized 'blob-like' structures in the images from NSTX are illustrated in figure 17. Here, a blob is defined as a strong local maximum in the He I light emission that moves over a distance larger than its own diameter (i.e. the red–white regions in these images). The images in figures 17(*a*)–(*c*) are from the Ohmic shots in table 1, while (*d*) was from a neutral beam heated case (fixed circles and diagonal lines have been added for reference). In (*a*), the blob moves radially outwards and then seems to disappear; in (*b*), the blob first moves radially outwards and then slightly upwards (electron diamagnetic drift direction); in (*c*), the blob moves radially outwards and then downwards; and in (*d*), the blob enters from the top of the image, moves downwards, then radially outwards and finally downwards. In general, these blobs move both radially and poloidally and change shape and size significantly over their lifetime within this field of view.

Some analysis of this type of blob motion is shown in figure 18, which is based on a set of 22 discharges (mostly from table 1). In each frame, a blob was operationally defined as any region above an arbitrary threshold (typically 0.7 times the maximum brightness in that region). The blobs were tracked over all frames in each shot, and their properties were collected in a database of 146 tracks, with an average length of 6–7 frames for each track. In the top row is the distribution of radial vs poloidal velocities of the blobs as determined from the relative motion of blob centres between two successive frames during the tracking of a blob. At the bottom is the radial velocity vs the intensity of the blobs, where the intensity is the average over these two frames normalized to the average over all (28) frames. The average blob area was 10–15 cm^2, and the average lifetime within this field of view was 60–70 μs.

The distribution of inferred blob velocities is rather broad, as shown at the top of figure 18, with mean velocity magnitudes of $|v_{\mathrm{pol}}| \approx 1.2 \times 10^5$ and $|v_{\mathrm{rad}}| \approx 0.5 \times 10^5\,\mathrm{cm\,s^{-1}}$, with slightly more blobs moving radially outwards (to the right) than inwards and more moving in the ion grad-B drift direction (downwards) than the electron drift direction. The poloidal velocity distributions increase slightly towards the ion drift direction during L- and H-mode plasmas. The radial and poloidal velocity distributions are similar in the Ohmic case, but in the L-mode and especially in the H-mode, the radial distribution appears to be narrower. However, this may in part be due to the narrower range of radii viewed by GPI in these cases; for example, in the H-mode any radial velocity $\geqslant 3\,\mathrm{cm}/10\,\mu\mathrm{s} \approx 3\,\mathrm{km\,s^{-1}}$ would be difficult to track since the radial range of the GPI images is only $\approx$3 cm wide (see figure 6). On the basis of the plots of intensity vs radial velocity at the bottom of figure 18, there seems to be no correlation between the radial velocity and intensity in this data set. Note that the radial particle transport due to these blobs cannot yet be determined without a clearer identification of the local density and radial velocity fluctuations since the local transport depends on the correlation between these two quantities (see section 4.4).

Much more analysis is required to determine the physical and statistical significance of these blobs and their motion. For example, it is not clear that all the local maxima tracked in figure 18 correspond to the density blobs discussed in recent theory [53] since the definition of a blob here is somewhat arbitrary and since the He I light emission is affected by temperature and neutral density variations as well as density fluctuations. Also, sometimes the light emission from a blob seems to increase or decrease over its lifetime (as in the first few frames of figure 19(*d*)), implying a change in the local density or temperature possibly due to transport of particles and/or heat along a field line (which is not measured in this experiment). In general, the identification of coherent structures also requires additional analysis to determine the extent to which such structures are statistically significant and not just due to random fluctuations.

Some examples of 'wave-like' motion in these images are shown in figure 19. Figure 19(*a*) shows an ELM-free H-mode discharge that had a spatially periodic edge mode, located a few centimetres inside the separatrix, with a poloidal wavelength

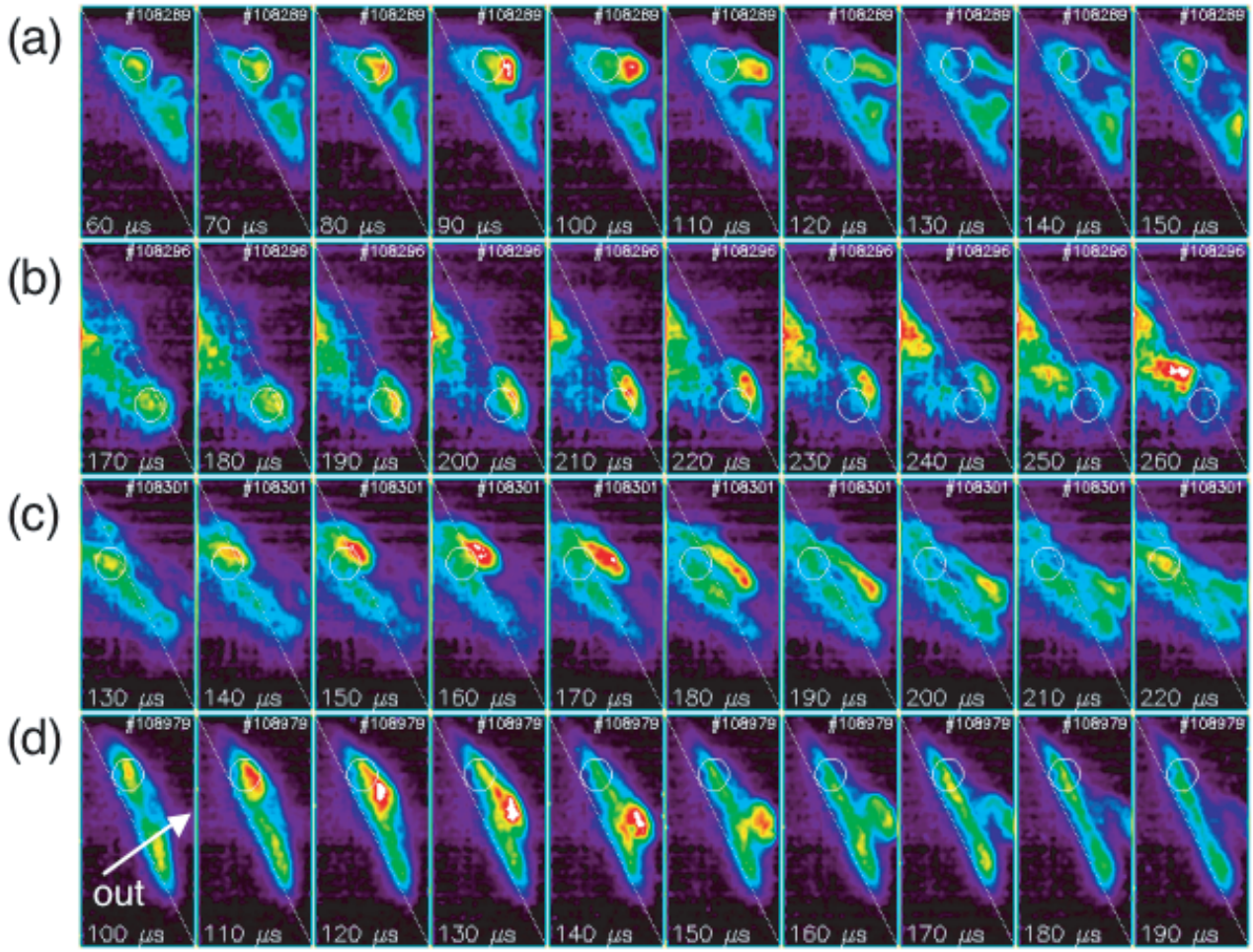

Figure 17. Examples showing the motion of localized structures or blobs in the He I light emission as seen in the PSI camera images taken at 10 μs frame^{-1}. Cases (*a*)–(*c*) are Ohmic discharges (#108289, 108296, 108301), and case (*d*) had 3.3 MW of NBI (#108979). The blobs move both radially and poloidally and change shape and size significantly over their lifetime within this field of view (fixed circles and diagonal lines have been added for reference). Only ten of the 28 frames in each shot are shown.

of ≈20 cm and a period of ≈100 μs. Figure 19(*b*) shows a continuation of this same sequence in which a blob forms and moves radially outwards. Figure 19(*c*) shows another ELM-free H-mode that has a similar wave-like structure but with blob-like maxima that move poloidally through the frames. Finally, figure 19(*d*) shows an L-mode case in which a blob at the lower right moves upwards along the diagonal line, while at the same time two blobs radially inside and outside of it move downwards along that line, all three crossing near the circle shown. This behaviour might be related to a 'zonal flow' in which oppositely directed poloidal flows are generated by the turbulence itself. These and other interesting structures and motions are most easily appreciated in the videos (see http://www.pppl.gov/∼szweben).

The periodic edge modes seen in figures 19(*a*) and (*c*) are not correlated with any MHD activity at the frequency of this wave (≈10 kHz), and so this structure is most likely a 'quasi-coherent' edge density fluctuation seen in DIII-D and Alcator C-Mod [25, 50]. In other discharges that have large coherent MHD activity in the H-mode (e.g. #108478), there is often a few centimetres radial oscillation of the He I light emitting region at the same frequency but without any poloidal variation, which is most likely due to the magnetic flux surface movements associated with these low-*n* MHD modes (e.g. tearing modes).

3.4. Other imaging results

Additional imaging and chord results were obtained using a deuterium puff with a D_α filter instead of the He puff with a He I (587.6 nm) filter used for sections 3.1–3.3. In general, the D_α images and time series results were similar to the He I results described above. For example, in a set of 10 discharges during a one run day with a deuterium GPI puff, the same image analysis as in section 3.1 (near the radial peak of the D_α images) showed a mean poloidal correlation length of 4 ± 0.5 cm and an rms fluctuation level of 0.09 ± 0.02. This is well within the range of the results of figure 7. Half these shots had an exposure time of 10 μs frame^{-1} (as for the He results) and half had an exposure time of 5 μs frame^{-1}, but the results were very similar with either gating time. The time series, autocorrelation functions, frequency spectra and PDFs of the fast chord signals in D_α were also similar to those seen in He I (figures 11 and 13). The spatial location of the D_α emission was similar to the He I emission, and the background D_α light

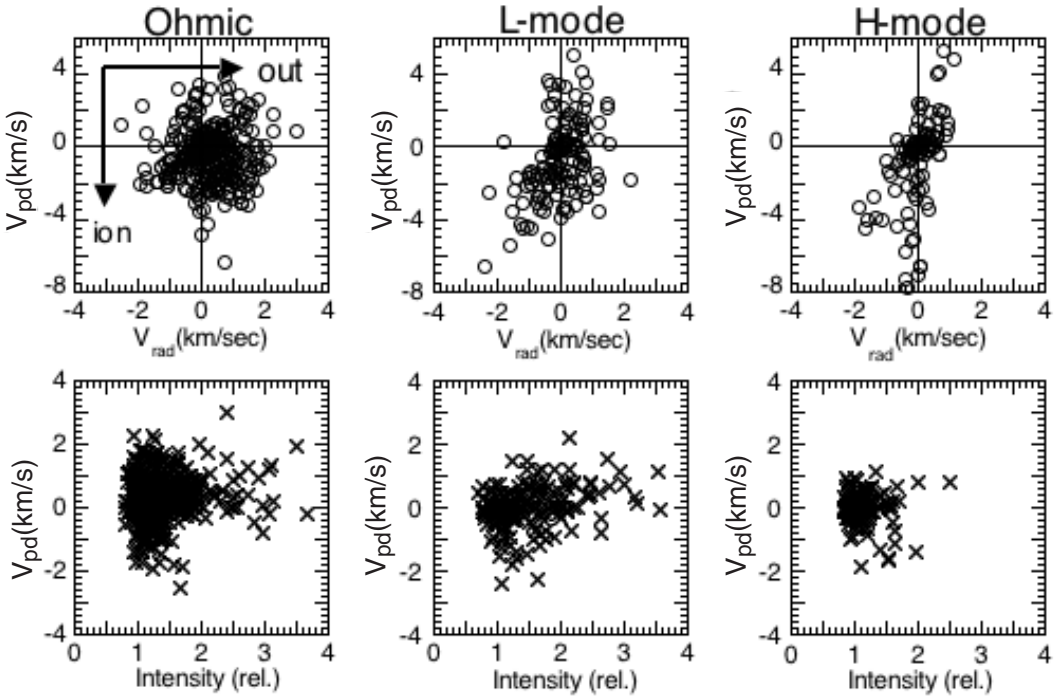

Figure 18. Analysis of blob motion in the PSI camera data for a total of 22 Ohmic, L- and H-mode discharges. In the top row are the instantaneous velocities of the blobs in the radial vs poloidal plane as determined from the relative motion of the local maxima between two successive frames (the radially outward and ion diamagnetic directions are shown at the upper left). At the bottom is the radial velocity vs the intensity of the blobs, where the intensity is the average over the two frames normalized to the average over all (28) frames.

level without the deuterium puff was ≈10% of the peak level during the deuterium puff.

When no optical filter and no gas puff were used, the resulting image was a combination of the natural radiation from the outer plasma edge and the recycling light from the wall tile surface near the upper divertor plate. Often, this image showed elongated filaments moving across the wall surface, similar to images made using a fast divertor camera in NSTX [54]. Sometimes it appeared as if these filaments were intersecting the tiles and 'splashing' over an area of several centimetres.

In preparation for a laser-induced fluorescence measurement of edge turbulence, an attempt was also made to image the singly ionized argon ion line. With the same argon gas pressure in the manifold as used for helium, the Ar II (488.2 nm) light was about four times dimmer than the He I (587.6 nm) light, and so images could be seen clearly only with a 20 μs exposure time. These images looked at least qualitatively similar to the images made in He and D, with localized structures moving poloidally and radially through the field of view. However, the radiation level appeared to increase significantly during the Ar puff and it is possible that was cooling the plasma edge.

4. Discussion

The measurements described in section 3 can in principle be used to test theoretical models of edge turbulence using an atomic/neutral physics model such as DEGAS 2 to calculate the expected He I light emission fluctuations based on theoretically predicted density and temperature fluctuations. This process has been attempted with some success in Alcator C-Mod [19] but has not yet been done for NSTX since theoretical simulations are not yet available. Of course, this comparison could only be made for statistical quantities such as correlation lengths and power spectra, although coherent structures could also be defined and compared as well.

This section will discuss several issues concerning interpretation of the experimental results of section 3. A numerical analysis of the general relationship between He I light fluctuations and plasma fluctuations is described in section 4.1. Comparisons of these GPI results with other edge fluctuation measurements in NSTX are described in section 4.2, comparisons with other experiments are described in section 4.3, comparisons with theory are discussed in section 4.4 and the conclusions are in section 4.5.

4.1. Simulation of He I fluctuations vs plasma fluctuations

The relationship between fluctuations in the He I light emission and the underlying electron density and temperature fluctuations depends upon the atomic physics of the specific transition, as discussed in section 2.2. At each point in radial profile, the emissivity can be approximated for a specific transition by $S \propto n_e^{\alpha} T_e^{\beta}$, where α and β are determined from a collisional radiative model of He I [36, 37]. An example of these exponents vs radius for a typical NSTX discharge is shown in figure 20(*a*), along with the calculated He I (587.6 nm) emission for this case (same discharge as for figure 3). Near the peak emission, these exponents are $\alpha \approx 0.5$ and $\beta \approx 0.7$, but they range over $-0.5 \leqslant \alpha, \beta \leqslant 4$ for the whole region of emission.

The effect of the atomic physics exponents on the structure of the observed turbulence was simulated by assuming the various one-dimensional k-spectra for the spatial structure of

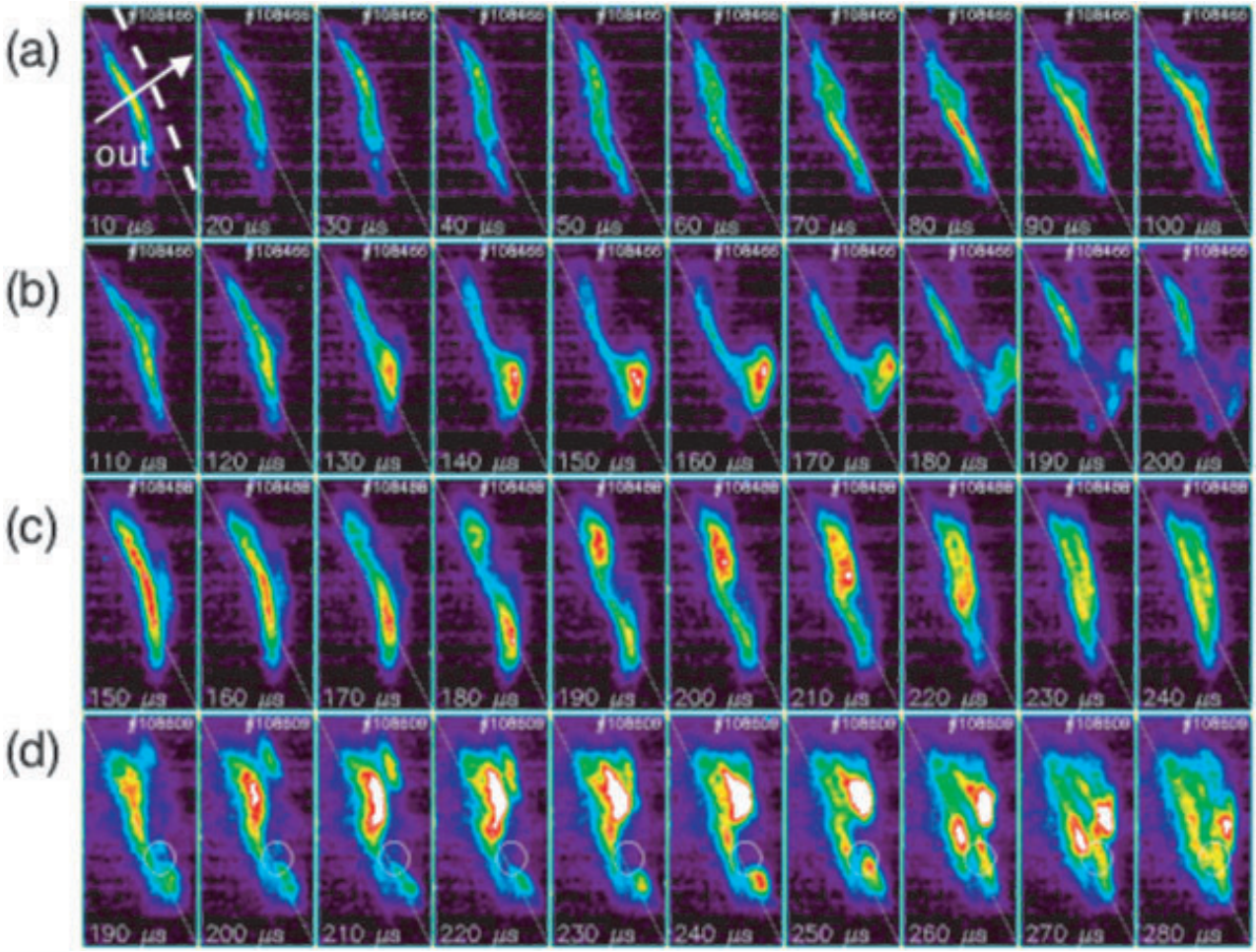

Figure 19. Examples of wave-like structure as seen in the PSI camera images taken at 10 μs frame^{-1}, where all shots had NBI at $I = 900$ kA. Case (*a*) is an H-mode with a radially oscillating periodic structure (#108466), case (*b*) shows the next ten frames from the same shot with a blob forming and moving outwards, case (*c*) is an H-mode with a poloidally modulated wave-like structure (#108488) and case (*d*) is an L-mode with counter-propagating blobs (#108609). The diagonal lines and fixed circles are for reference, and the EFIT separatrix location is shown for case (*a*) in the first frame.

$\tilde{n}$, as shown in figure 20(*b*). For each spectrum, the relative correlation lengths and fluctuation levels of the resulting emissivity, $S = \tilde{n}_e^{\alpha}$, were calculated as a function of α by averaging over an ensemble of the assumed k-spectra with random phases and a total rms fluctuation level of ≈24%. The calculated correlation lengths of the resulting emissivity were found to be nearly independent of the assumed α over the range $-2 \leqslant \alpha \leqslant 4$, as shown in figure 20(*c*), while the relative fluctuation level varied nearly linearly with $|\alpha|$, as shown in figure 20(*d*). In addition, the calculated k-spectrum of the emissivity is also approximately the same as the assumed k-spectrum of $\tilde{n}$, as illustrated by the dashed line corresponding to case (1) of figure 20(*b*). Finally, the calculated correlation lengths are approximately invariant even when α is varied over space in this range, as it would be for the radial correlations (after normalizing to the average values at each point, as done in the data analysis). A similar set of conclusions applies to the T_e dependence of S (i.e. β).

Thus, the correlation lengths and k-spectra of the measured He I light emission should be very similar to those of the underlying turbulence, assuming that the density and temperature fluctuations are approximately in phase, as expected theoretically for $E \times B$ driven advection and sometimes observed experimentally [26, 40]. Also, since k-space is identical to frequency space in this numerical simulation, the autocorrelation times and frequency spectra of the measured He I light emission should also be very similar to those of the underlying turbulence. Exceptions to this would occur for the unlikely cases where $\alpha + \alpha_T \approx 0$ or where the density and temperature fluctuations had different spectra.

On the other hand, the interpretation of the relative fluctuation levels of He I light emission will depend on the assumed α and β, which in turn will depend on the details of the density and temperature profiles. If the density fluctuations dominate the temperature fluctuations, then the measured He I profiles should be similar to the underlying $\tilde{n}$ profiles since $0.5 \leqslant \alpha \leqslant 1$. However, in general the quantitative interpretation of fluctuation levels from GPI measurements is difficult without a more accurate measurement of the average temperature and density profiles.

Simulations of the two-dimensional spatial structure of the underlying turbulence and the resulting He I light emission show that there is an increased rms fluctuation level for large 'α', as in figure 20(*d*), but also an increase in the intermittency

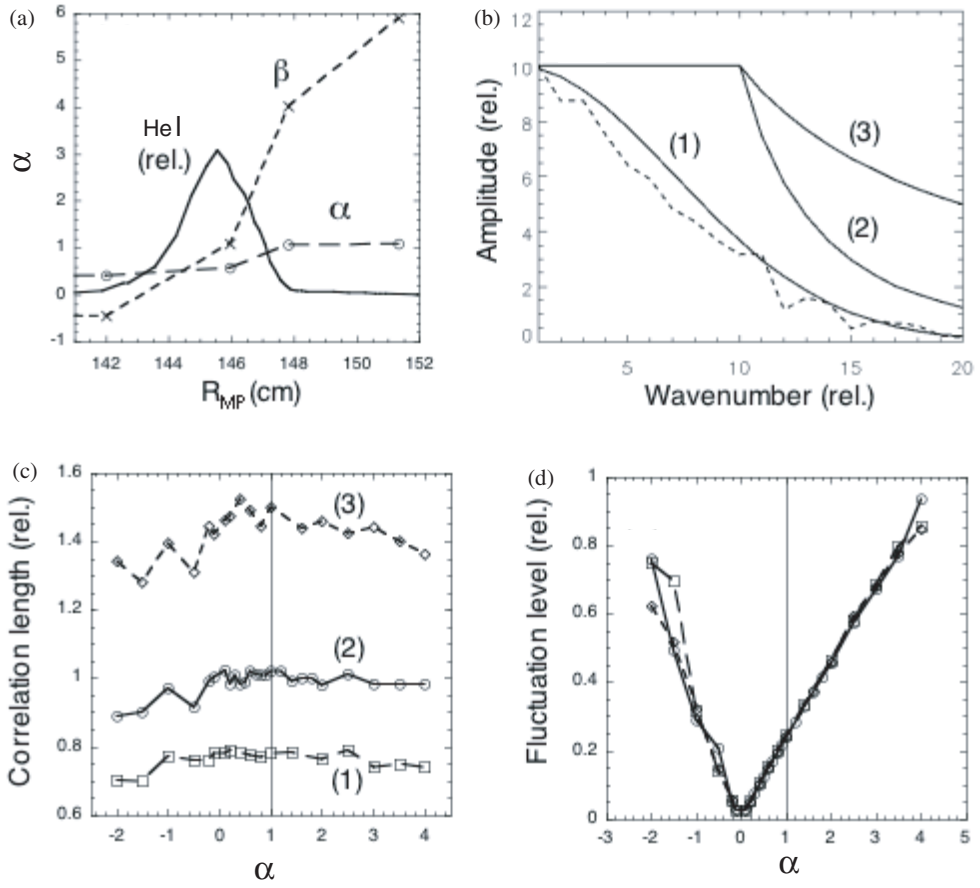

Figure 20. Numerical simulations of the relationship between an assumed spectrum of density fluctuations, $\tilde{n}$, and the corresponding He I light emission, $S \propto \tilde{n}^{\alpha}$. In part (*a*) are the calculated He I radial profile and local exponents of density and temperature for a typical NSTX discharge (#108322). In part (*b*) are three assumed $\tilde{n}(k)$ for these simulations. In part (*c*) are the calculated correlation lengths of S as a function of the assumed exponent, α, averaged over ten realizations with random phases for each k and an average fluctuation level of 24% (rms/mean). In part (*d*) are the calculated fluctuation levels (rms/mean) vs α. The calculated $S(k)$ for spectrum (1) with $\alpha = 2$ is shown by the dashed line in part (*b*), averaged over 100 realizations.

of the images due to $\delta S/\delta n \propto |\alpha|$. Thus, the PDFs of the measured He I light (e.g. in figure 13) can be sensitive to the atomic physics; for example, a non-Gaussian PDF may in part be due to the sensitive dependence of He I emission on temperature fluctuation at low T_e. However, the local maxima retain their identity independent of α, and so the gross structure of the two-dimensional images and the tracking of blobs should be fairly independent of the atomic physics.

One area of interpretation not accounted for in these simple simulations is the dependence of the He neutral fraction on the radius, as illustrated in figure 3. To a first approximation, the neutral density is constant at each point in space, and so its value should not affect the interpretation of the relative fluctuations in He I light emission. However, some nonlinear interaction between the fluctuations and the neutral density is possible for large fluctuation levels, as discussed in section 2.2. Simulations of this effect made using DEGAS 2 have so far shown that the spatial structure of the fluctuations is relatively insensitive to this effect [39, 40].

4.2. Comparisons with other NSTX diagnostics

This section presents some comparisons of the GPI results of section 3 with other available information on edge fluctuations in NSTX. At present there is at least qualitative agreement among these diagnostics, but detailed quantitative comparisons are difficult and beyond the scope of this paper.

The most direct comparison of GPI is with the fast divertor camera, which viewed the toroidal vs poloidal structure of the D_α recycling light near the bottom of the NSTX vessel at $\leqslant$40 000 frames s^{-1} [54]. These images showed fluctuating 'filaments' of light emission a few centimetres wide in the poloidal direction aligned nearly along the magnetic field, which were stronger in the L-mode than the H-mode. This is at least qualitatively similar to the GPI results, even though the spatial location of the GPI measurements was different. The divertor camera also showed variations in this filamentation with different types of ELMs, which has not yet been seen in the GPI images.

A comparison was also made between GPI and edge Thomson scattering data in NSTX. For some of the discharges of table 1, the two Thomson scattering laser pulses (each 8 ns wide) were fired 400 μs apart during the GPI measurement so that the short-timescale variations in electron density, n, and electron temperature, T, could be measured (each channel viewed an area $<$1 cm poloidal by 1–1.5 cm radial). Since this time difference is larger than the autocorrelation time and shorter than the discharge evolution timescale, these

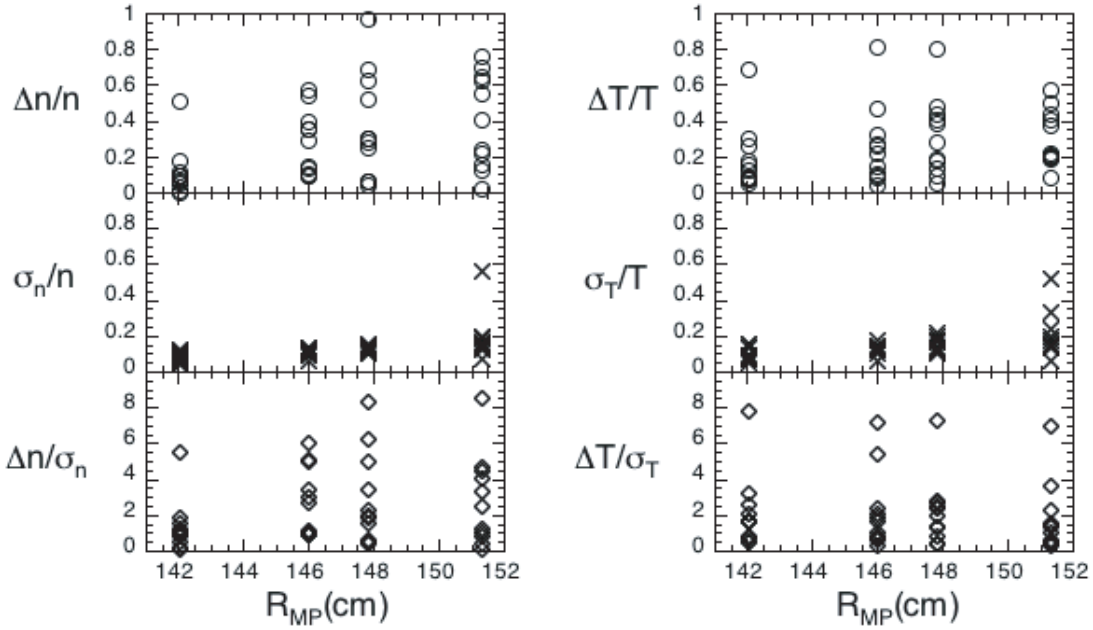

Figure 21. Fluctuation analysis of the edge Thomson scattering data for 11 shots of table 1. The top panels show the measured differences, Δn and ΔT_e, between two laser pulses 0.4 ms apart, normalized to their average. The middle panel shows the expected photon-statistical fluctuations in these differences normalized to their average and the bottom panel shows these measured differences normalized to the expected photon-statistical fluctuation levels. The measured variations in n and T_e are about twice the expected statistical variation, implying a significant edge fluctuation level.

fluctuations are most likely due to edge turbulence (although MHD effects are not excluded). At the top of figure 21 are radial profiles of the relative variations between these two time points, i.e. $\Delta n/n$ and $\Delta T/T$, as a function of the major radius, R_{MP}, where n and T are the average values over the two times. These relative fluctuation levels as measured by Thomson scattering are ≈10–60%, which is roughly consistent with the fluctuation levels seen in GPI for these shots (see figure 7). In the middle of figure 21 are the expected photon-statistical fluctuation levels in these measurements, i.e. σ_n/n and σ_T/T, where these σs are the square roots of the sums of the squares of the error bars of the two individual measurements (not including the uncertainty in the mean value, which increases σs negligibly). At the bottom is the measured time variation normalized to the statistical uncertainty. Thus, the measured variations are statistically significant; for example, at $R_{MP} = 146$ and 148 cm, about two-thirds of the points in the bottom graph are above one for both n and T (only one-third of the points should be above one standard deviation due to statistical uncertainty). The signs of these variations are equally positive and negative, as expected for turbulent fluctuations, but interestingly there was no apparent correlation between the signs of Δn and ΔT in these data (if true, this might complicate the GPI interpretation). Similar strong edge fluctuations on a fast timescale have also been seen in the Thomson scattering measurements in ASDEX Upgrade [55].

Another diagnostic comparison was made between GPI data and the ORNL edge reflectometer system [56], which consists of an x-mode reflectometer at the outer midplane that can be run at two different frequencies for measuring edge turbulence. The power spectra of the reflectometer phase fluctuations for a cutoff density near 3.5×10^{12} cm^{-3} is shown in figure 22, along with the power spectra from a GPI fast

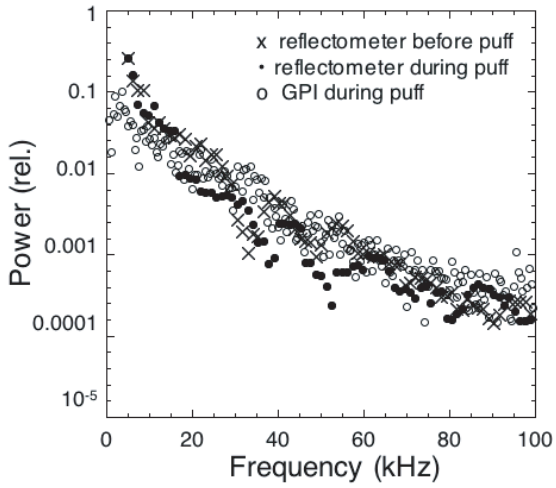

Figure 22. Comparison of the edge turbulence power spectra measured by the ORNL reflectometer and the GPI fast chords during a typical NSTX L-mode shot (#108980). The reflectometer data labelled with an 'x' were taken just before the GPI He puff, while the reflectometer data labelled with a '●' were taken during a GPI He puff. This reflectometer channel has a cutoff at 3.5×10^{12} cm^{-3}, which roughly corresponds to the location of the GPI chord shown ($R_{MP} \approx 150$ cm). The spectra of the reflectometer signals and GPI signals are roughly similar, as are the reflectometer signals before (0.268 s) and during (0.288 s) the He puff. The reflectometer spectra have the same gain, and the GPI spectra are normalized in amplitude to the reflectometer spectra.

chord localized at a similar radius (near $R_{MP} = 150$ cm for this L-mode, shot #108980). The GPI and reflectometer power spectra have a similar shape over the frequency range 1–100 kHz, although there is somewhat more power below 10 kHz in the reflectometer. Also, the reflectometer signals

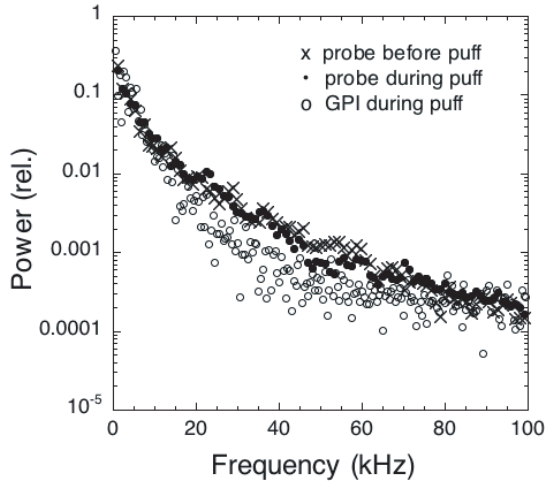

Figure 23. Comparison of the edge turbulence power spectra measured by the UCSD fast probe and a GPI edge channel for typical H-mode shots in NSTX. The probe data for the shot labelled with 'x' were taken just before the GPI He puff (#109039 at 0.31 s), while the probe data labelled with '●' were taken during a GPI He puff (#109037 at 0.41 s). All spectra are normalized to have the same total power between 1 and 100 kHz. The GPI spectrum was obtained from 10 000 points for shot #109039 between 0.35 and 0.37 s at $R = 150$ cm. The spectra of the probe signals and GPI signals are roughly similar, and the probe signals are similar with and without the He puff.

are very similar before and during the GPI He puff (0.268 vs 0.288 s), showing that the He puff is not affecting the edge turbulence measured by this reflectometer. Similar results were obtained in the lower frequency reflectometer channel.

Finally, a preliminary comparison was made between the GPI data and the edge turbulence as measured by the UCSD fast Langmuir probe, which was able to penetrate transiently to just outside the separatrix near the outer midplane. The power spectra of ion saturation current fluctuations from this probe are shown in figure 23, along with the power spectra from a GPI fast chord, both for typical H-mode shots (#109037, 39). The shapes of the GPI and probe power spectra are similar over the frequency range 1–100 kHz, although the GPI signals are somewhat lower in the ≈30–50 kHz range. The probe spectra are similar with and without the GPI He puff, showing that the He puff is not significantly affecting the edge turbulence as measured by this probe. The relative fluctuation level seen in the ion saturation current was ≈0.8–1.0, which was comparable with that seen in the GPI (e.g. figure 12).

4.3. Comparison with other experiments

A large number of edge turbulence measurements have been made using a variety of techniques on many different devices, as reviewed in [1–4]. In general, these measurements of edge turbulence in NSTX are qualitatively similar to the previous measurements, e.g. showing large edge fluctuation levels with broadband spectra in the frequency range ≈1–100 kHz. Some differences are to be expected due to the low-aspect ratio of NSTX, and other differences are expected since each type of diagnostic provides a somewhat different characterization of the turbulence.

The GPI diagnostic of edge turbulence has been used in only one other device so far, namely Alcator C-Mod [19], using mainly deuterium gas and a D_α filter. The edge turbulence images in C-Mod look qualitatively similar to those seen in NSTX, but the correlation lengths are significantly smaller in C-Mod, i.e. $L_{\rm pol} \approx 1$ cm in C-Mod vs $L_{\rm pol} \approx 4$ cm in NSTX; also, the autocorrelation times are significantly shorter, i.e. $\approx 10\,\mu$s in C-Mod vs $\approx 40\,\mu$s in NSTX. This trend towards longer correlation lengths at lower B fields is consistent with drift wave scaling and many previous results [1–4, 34, 35]. Both NSTX and Alcator C-Mod showed highly localized coherent structures ('blobs') that move both poloidally and radially through the edge, with a preference for radially outward motion in the SOL.

The time-averaged two-dimensional structure of the edge turbulence in NSTX is approximately isotropic in the plane perpendicular to B (figure 9), somewhat in contrast to Langmuir probe measurements in tokamaks and stellarators that previously showed a longer poloidal correlation length than radial correlation length [12, 13, 15]. This is perhaps due to the different magnetic geometry of NSTX, which has a much larger ratio of poloidal field to toroidal field at the outer midplane. However, the shapes of the k-spectra in figure 8 are at least qualitatively similar to those measured with previous imaging systems in TEXTOR [15], C-Mod [19] and with probes [23, 33].

Edge turbulence has been measured near the outer midplane of DIII-D using both Langmuir probes and BES [25–27]. The probes revealed strongly intermittent turbulence in the SOL, while the BES detected localized perturbations moving poloidally and radially near the separatrix. These 'IPOs' in the SOL were characterized by non-Gaussian PDFs, similar to the GPI time series results in figure 13. The motion of IPOs was measured using conditional sampling of probe data and showed a radial speed of 0.3–3 km s^{-1}, which is similar to the radial blob speeds in NSTX (figure 18), and the spatial scale of the structures seen with BES is ≈2 cm, which is somewhere between the size of those seen in NSTX and in Alcator C-Mod. Qualitatively similar intermittent turbulence structures have been seen in non-fusion devices such as Blaamann [29], MIRABELLE and TEDDI [31] and PISCES [32].

The average edge turbulence level in the H-mode is somewhat smaller than in the L-mode in NSTX (figure 7), as with probe measurements in DIII-D [25–27] and PBX-M [57]. However, GPI measurements in Alcator C-Mod showed nearly the same fluctuation level in H- and L-modes [19], probably because those measurements were in the SOL, whereas the GPI measurements in NSTX were often near or inside the separatrix. The poloidal correlation lengths of edge turbulence in L- and H-modes were similar in NSTX (figure 6), as were radial correlation lengths in L- and H-mode edge plasmas in ASDEX [58].

The wave-like structures in the H-modes seen in figure 19 may be related to the quasi-coherent mode observed in H-mode plasmas in tokamaks [26, 50, 57] (also sometimes called an edge localized oscillation or EDA mode). The distinguishing features of this mode are its edge localization and its nearly monochromatic frequency spectrum. In NSTX, this mode is identified by its periodic poloidal structure with a wavelength of ≈20 cm, in contrast with the usual incoherent turbulent structure in NSTX with a correlation length of ≈4 cm. The cause of this mode in NSTX is presently unknown.

4.4. Connections to theoretical models

It is clear that quantitative connections to specific theoretical models must be made in order to understand and interpret the results of this paper. The best quantitative connection would be a comparison of these imaging results with turbulence simulation results from codes such as described in [5–11], although qualitative connections with simplified theoretical models would perhaps be more useful in understanding the basic physics.

For example, BOUT [6] is a boundary turbulence code that calculates the nonlinear saturated state of edge turbulence in diverted toroidal plasmas on the basis of a three-dimensional nonlinear two-fluid (collisional) model, given the time-averaged plasma edge profiles and magnetic geometry. A BOUT simulation made for the outer midplane of NSTX using generic edge profiles [6] has already produced several results similar to the measured edge turbulence, namely (a) the turbulence size scale perpendicular to B was a few centimetres in both the radial and poloidal directions, while the parallel correlation length was many metres, (b) the autocorrelation time was ≈10–30 μs and the frequency spectrum was close to that observed in the fast chord signals and (c) fluctuation levels in the edge were typically in the range of $\geqslant$10%.

Future comparisons of turbulence simulation codes with the NSTX data can begin as in [19], in which the GPI results from Alcator C-Mod were compared with the NLET edge turbulence simulation code. In that case, the edge density and temperature profiles and magnetic geometry from a specific shot were used as initial conditions in the code, which was then run until the nonlinear saturated state was reached. The resulting spectrum of edge density and temperature fluctuations was then used to calculate the expected GPI light fluctuations on the basis of the known atomic physics curves for the light emission vs density and temperature. Finally, the k-spectra of the GPI measurement were directly compared with those from the simulation code; the result was an encouraging (but not complete) level of agreement. A similar procedure can be used to compare other statistical quantities such as the relative fluctuation levels, frequency spectra and various statistical moments (e.g. PDF, skewness, kurtosis, etc). This procedure will of course be limited by the accuracy of the measurements of the time-averaged edge profiles used as input to the code and by the limited data from the finite number of turbulence images in a given discharge. However, basic trends such as the variations with L- and H-modes, with density and with the various dimensionless edge parameters (table 2) should be discernable in such comparisons.

More sophisticated analysis techniques will be needed to compare coherent structures in experiment and simulation. The main difficulty here is that there is no *a priori* definition of coherent structures in fluids [47, 48] or plasmas, and so these structures must first be suggested from the data, from the theory or from the simulation. Once a quantitative definition has been established, it should be straightforward to compare experiment and simulation, as described in the previous paragraph. For example, the blob tracking method used for the NSTX data in figure 18 can be applied to the simulation results after correction for the atomic physics effects.

Another general approach to experiment–theory comparison is to use simplified analytic models rather than a full turbulence simulation to interpret the data. For example, a relatively simple model for SOL blobs [53] can be tested with the imaging data from this experiment, as perhaps could a dynamic 'predator–prey' model of drift wave-zonal flow turbulence [59]. Other theoretical ideas that could be examined concern self-organized criticality (SOC) [60], the effect of the divertor plate contact on turbulence in the SOL [61], the interplay between self-generated zonal flows and intermittent transport events [9] and the effect of flux-driven (as opposed to gradient-driven) turbulence [10].

In the absence of quantitative theoretical comparisons, some ordering of the data can also be obtained by comparing them with simple theoretical scalings for edge turbulence such as those discussed previously [1–4, 33, 34]. For example, the usual drift wave scaling, $k_{\rm pol}\rho_{\rm s} \approx 0.2$, is approximately consistent with the measured $k_{\rm pol} \approx 1\,{\rm cm}^{-1}$ (figure 7) and $\rho_{\rm s} \approx 0.2$ cm in NSTX (table 2). Similarly, the usual 'mixing length' estimate, $\tilde{n}/n \approx 1/k_{\rm rad}L_{\rm n}$, is roughly consistent with the typical fluctuation level in NSTX of $\delta I/I \approx 50\%$ (figure 6) with $k_{\rm rad} \approx 1\,{\rm cm}^{-1}$ and $L_{\rm n} \approx 2$ cm (table 1). The resistive ballooning mode (RBM) scale length in NSTX for the parameters of table 2 is $L_{\rm RBM} = 1$ cm, which is about one-fourth the observed correlation length in NSTX. However, it is clear from previous work [19] that the linear instability scale length is not necessarily the same as the nonlinear correlation length of the RBM turbulence.

Finally, the radial transport due to the motion of this edge turbulence cannot yet be determined directly from these imaging data since the light fluctuations would need to be unfolded in terms of their local density and temperature fluctuations. However, it should be possible to estimate the local velocity fluctuations from these data and compare them with theoretical simulations, e.g. to determine the local vorticity or divergence. This should help determine whether the edge turbulence was associated primarily with drift waves, interchange modes or possibly with other physical effects.

4.5. Conclusions

This paper described high-speed two-dimensional imaging of the edge turbulence in NSTX made using a GPI diagnostic, which measured the fluctuations in He I light emission in the region where $T_{\rm e} \approx 5$–50 eV near the outer midplane separatrix. Simple modelling showed that the space–time structure of the measured He I light emission should be similar to that of the underlying plasma density and temperature fluctuations.

The main results of this paper can be summarized as follows:

(a) the poloidal correlation lengths of edge turbulence as seen by GPI were $L_{\rm pol} \approx 4 \pm 1$ cm in Ohmic, L- and H-mode plasmas (figure 7), and the shapes of the poloidal k-spectra were similar in these three regimes (figure 8),

(b) the edge turbulence seen by GPI often had an intermittent character, with a non-Gaussian PDF in the outer edge (figure 13) and with localized coherent structures seen moving through the edge in two dimensions (figures 17 and 18),

(c) the relative fluctuations levels were lower on average in the H-mode than in the L-mode or Ohmic plasmas (figure 7), with intermittent coherent structures appearing during the H-mode even without the presence of ELMs (figure 16),

(d) H–L and L–H mode transitions were seen as very rapid ($\leqslant 100\,\mu$s) changes in the GPI signal levels and relative fluctuation levels (figures 14 and 15),
(e) the frequency spectrum of the GPI fluctuations was similar to that of the edge reflectometer and Langmuir probes (figures 22 and 23) and consistent with fluctuations seen in the Thomson scattering diagnostic (figure 21).

So far, the edge turbulence measured near the outer midplane of NSTX appears to be qualitatively similar to the edge turbulence seen previously in larger-aspect ratio tokamaks or stellarators. This is too not surprising, given the similarity of edge turbulence seen in many other types of magnetized plasmas. However, many possible influences on edge turbulence in NSTX remain to be explored, for example, the effects of plasma rotation, RF heating, impurity content, magnetic geometry and wall surface conditions.

Many open questions also remain concerning the physics of edge turbulence in general. It is not yet clear what the dominant driving and damping mechanisms are for this turbulence, and so careful scans and comparisons with theoretical simulations are needed. The cause of the H-mode transition is still unclear, and so it would be very useful obtain two-dimensional images that capture the L–H and H–L transitions and to compare these with theory. The density limit is not understood, and so the density scan should be pushed nearer the experimental density limit. The causes of the intermittent coherent structures need to be clarified both experimentally and theoretically.

Perhaps the most important open issue concerns the general relationship between the edge profiles, edge turbulence and edge transport since the edge conditions are known to affect both the plasma–wall interactions and the global plasma performance. For example, the larger than expected cross-field particle transport recently observed in the SOL [62] can strongly increase the main chamber recycling and affect the design of future tokamak divertors. It would also be useful to develop active edge turbulence control methods that could clarify these relationships, and to couple edge turbulence models to core turbulence models for a more complete simulation of turbulent transport.

Acknowledgments

This work was performed under DOE contract #DE-AC02-76CHO3073. Amy Keesee was supported by a DOE Fusion Energy Sciences Fellowship. We thank the following people for valuable discussions and/or support for this work: M. Bell, R. Bell, B. Davis, D. D'Ippolito, E. Fredrickson, M. Gilmore, T. S. Hahm, K. Hallatschek, G. Hammett, D. Johnson, R. Kaita, S. Kubota, H. Kugel, B. LaBombard, F. Levinton, J. Myra, W. Nevins, M. Ono, M. Peng, B. Rogers, L. Roquemore, S. Sabbagh, J. Strachan, D. Stutman, E. Synakowski, J.L. Terry, G. Wurden and X. Xu.

References

[1] Endler M. 1999 *J. Nucl. Mater.* **266–269** 84
[2] Carreras B.A. 1997 *IEEE Trans. Plasma Sci.* **25** 1281
[3] Wootton A.J. *et al* 1990 *Phys. Fluids* B **2** 2879
[4] Liewer P.C. 1985 *Nucl. Fusion* **25** 543
[5] Rogers B.N., Drake J.F. and Zeiler A. 1998 *Phys. Rev. Lett.* **81** 4396
[6] Xu X.Q. *et al* 2002 *New J. Phys.* **4** 53.1
[7] Scott B.D. 2003 *New J. Phys.* **4** 52.1
[8] Hallatschek K. and Zeiler A. 2000 *Phys. Plasmas* **7** 2554
[9] Beyer P. *et al* 2000 *Phys. Rev. Lett.* **85** 4892
[10] Sarazin Y. and Ghendrih Ph. 1998 *Phys. Plasmas* **5** 4214
[11] Benkadda S *et al* 2001 *Nucl. Fusion* **41** 995
[12] Zweben S.J. and Gould R.W. 1985 *Nucl. Fusion* **25** 171
[13] Bleuel J. *et al* 2002 *New J. Phys.* **4** 38.1
[14] Martines E., Hron M. and Stockel J. 2002 *Plasma Phys. Control. Fusion* **44** 351
[15] Huber A., Nedospasov A.V., Samm U. and Schweer B. 1999 *J. Nucl. Mater.* **266–269** 546
[16] McKee G.R. *et al* 2003 *Phys. Plasmas* **10** 1712
[17] Maqueda R.J. *et al* 2001 *Rev. Sci. Instrum.* **72** 931
[18] Zweben S.J. *et al* 2002 *Phys. Plasmas* **9** 1981
[19] Terry J.L. *et al* 2003 *Phys. Plasmas* **10** 1739
[20] Maqueda R.J. *et al* 2003 *Rev. Sci. Instrum.* **74** 2020
[21] Sykes A. *et al* 2001 *Nucl. Fusion* **41** 1423
[22] Zweben S.J. and Medley S.S. 1989 *Phys. Fluids* B **1** 2058
[23] Endler M. *et al* 1995 *Nucl. Fusion* **35** 1307
[24] Thomsen H. *et al* 2002 *Phys. Plasmas* **9** 1233
[25] Boedo J. *et al* 2001 *Phys. Plasmas* **8** 4826
[26] Rudakov D.L. *et al* 2002 *Plasma Phys. Control. Fusion* **44** 717
[27] Boedo J. *et al* 2003 *Phys. Plasmas* **10** 1670
[28] Chen F.F. 1965 *Phys. Rev. Lett.* **15** 381
[29] Fredriksen A. *et al* 2003 *Phys. Plasmas* **10** 4335
[30] Pedrosa M.A. *et al* 1999 *Phys. Rev. Lett.* **82** 3621
[31] Grulke O. and Klinger T. 2002 *New J. Phys.* **4** 67.1
[32] Antar G.Y. *et al* 2003 *Phys. Plasmas* **10** 419
[33] Zweben S.J. and Gould R.W. 1983 *Nucl. Fusion* **23** 1625
[34] Rhodes T.L, Ritz C.P. and Bengtson R.D. 1993 *Nucl. Fusion* **33** 1147
[35] Wootton A.J. *et al* 1992 *Plasma Phys. Control. Fusion* **34** 2023
[36] Fujimoto T. 1979 *J. Quant. Spectrosc. Radiat. Transfer* **21** 439
[37] Goto M. 2003 *J. Quant. Spectrosc. Radiat. Transfer* **76** 331
[38] Stotler D.P. and Karney C.F.F. 1994 *Contrib. Plasma Phys.* **34** 392
[39] Stotler D.P., LaBombard B., Terry J.L. and Zweben S.J. 2003 *J. Nucl. Mater.* **313–316** 1066
[40] Stotler D.P. *et al* 2004 Three dimensional neutral transport simulations of gas puff imaging experiments *Contrib. Plasma Phys.* submitted
[41] Meier M.A. *et al* 2001 *Phys. Rev. Lett.* **87** 500
[42] Maingi R. *et al* 2003 *Nucl. Fusion* **43** 969
[43] Reiser D. and Tokar M.Z. 2002 *Contrib. Plasma Phys.* **42** 401
[44] Pedrosa M.A. *et al* 1995 *Phys. Plasmas* **2** 2618
[45] Greenwald M. 2002 *Plasma Phys. Control. Fusion* **44** R27
[46] Bush C.E. *et al* 2003 *Phys. Plasmas* **10** 1755
[47] Schoppa W. and Hussain F. 2002 *J. Fluid Mech.* **453** 57
[48] Zabusky N.J. 1999 *Ann. Rev. Fluid Mech.* **495** 536
[49] Zweben S.J. 1985 *Phys. Fluids* **28** 974
[50] Mazurenko A. *et al* 2002 *Phys. Rev. Lett.* **89** 225004-1
[51] Jakubowski M., Fonck R.J. and McKee G.R. *Phys. Rev. Lett.* **89** 26500
[52] Politzer P.A. *et al* 2002 *Phys. Plasmas* **9** 1962
[53] D'Ippolito D. and Myra J. 2003 *Phys. Plasmas* **10** 4029
[54] Nishino N. *et al* 2002 *J. Plasma Fusion Res. (Japan)* Rapid Communication RC 0030, December 2002, http://jspf.nifs.ac.jp/RCPDF/
[55] Jacobi M. *et al* 2002 *29th EPS Conf. on Plasma Phys. and Control. Fusion (Montreux, 17–21 June 2002)* vol 26B (ECA) P-1,122
[56] Wilgen J.B *et al* 2002 *Bull. Am. Phys. Soc.* **47** 171
[57] Tynan G. *et al* 1994 *Phys. Plasmas* **1** 3301
[58] Kurzan B. *et al* 2000 *Plasma Phys. Control. Fusion* **42** 237
[59] Malkov M.A., Diamond P.H. and Rosenbluth M.N. 2001 *Phys. Plasmas* **8** 5073
[60] Garcia L., Carreras B.A. and Newman D.E. 2002 *Phys. Plasmas* **9** 841
[61] Nedospasov A.V. 1992 *J. Nucl. Mater.* **196–198** 90
[62] LaBombard B. *et al* 2001 *Phys. Plasmas* **8** 2107